

DAMPING PROPERTIES OF CONCRETE WITH SAND COATED RUBBER AGGREGATES

Yisihak Gebre ^{1*}, Tom Lahmer ², Matthias Müller³, Abrham G. Tarekegn ⁴and Esayas Gebreyouhannes ⁵

^{1,2}Bauhaus-Universität Weimar, Institute of Structural Mechanics, Germany

³Bauhaus- Universität Weimar, Institute for Building Materials Science, Germany

^{1,4,5} School of Civil and Environmental Engineering, Addis Ababa Institute of Technology, Addis Ababa University, Ethiopia

*Corresponding Author's E-mail: yisihakgebre@aait.edu.et

ABSTRACT

Waste tire rubber disposal causes major environmental problems and serious threats to human health around the world. A viable solution for reducing waste tire rubber is to reuse the material in concrete production. Since ordinary concrete is brittle, and has low energy absorption capacity, elastic rubber could possibly improve the damping behavior of concrete. In this study, the mechanical and dynamic properties of concrete with partial replacement of coarse aggregate by rubber and epoxy-sand coated rubber at different volume fractions ranging from 5 to 25% were investigated. Test results indicate that uncoated rubber chips in concrete causes a significant reduction in strength. As the bond between rubber particles and concrete matrix is typically weak, a new coating approach using epoxy-sand was applied to improve the interfacial properties of the rubber. Test results showed that an optimum compressive strength was achieved with 15% epoxy-sand coated rubber aggregate replacement. Furthermore, the maximum increment in damping ratios for uncoated and epoxy-sand coated rubber aggregates were found to be 58% and 23%, respectively as compared to normal concrete. Hence, the utilization of epoxy sand coated rubber presents a promising approach to enhance the dynamic performance of concrete structures, without affecting their mechanical properties.

Key Words: waste tire; epoxy, sand coated rubber; damping ratio; dynamic properties

1. INTRODUCTION

According to several studies, about 1.0 to 1.5 billion waste tires are discarded each year globally [1-3]. Scrap tires represent about 12% of all solid waste material [4]. Their disposal is thus a serious ecological and environmental issue, so it should be addressed by intensified recycling and reuse, which can create a sustainable environment and help to reduce landfill.

In Ethiopia, the amount of waste tire is increasing every year. Horizon Addis Tyre Factory has the capacity to manufacture around 850,000 tires a year [5]. According to the factory market demand prediction, Ethiopia's annual tire demand is estimated around 1.6 million pieces [6]. An estimated amount of at least one million waste tires is discarded every three years, resulting approximately ten thousand tons of waste tires annually [7, 8].

In earthquake prone areas, the use of concrete with good damping properties is necessary. Hence, a potential elastic material which has good abilities to dissipate impact energy is waste tire rubber.

Several researchers have used waste tire rubber as chipped (to replace the gravel),

crumb (replaces sand) and ground rubber (filler) for the production of so-called “rubberized” concrete [8-10]. The rubber material is characterized of low unit weight, high dynamic modulus and damping, low thermal conductivity and very low water absorption rate. It is a non-biodegradable material [11].

Studies mainly indicate that the utilization of waste tire rubber as coarse aggregate in concrete reduces the compressive, tensile and flexural strength of the modified concrete [12-16]. One of the main causes was adhesion failure between the surface of the rubber and the hardened cement paste [17-20]. Moreover, the partial replacement of fine aggregate by rubber was found to strongly decrease compressive and flexural strength of concrete [20].

A weakening effect was also found with regard to the modulus of elasticity of concrete [21-23]. For instance, in the case of 5% to 10% replacement of coarse aggregate by chipping rubber, a reduction in modulus of elasticity from 17% to 25% was observed [9]. Similar trends were seen in concrete with rubber powder as partial replacement for fine aggregate [16].

The compressive strength of concrete decreases as the percentage replacement of coarse aggregates with shredded rubber increases. The flexural strength increases when the contents of shredded rubber increases. Moreover, the modulus of elasticity of concrete decreases with the increase in percentage replacement of shredded rubber aggregates [24,25]. However, it was also reported occasionally, that the use of shredded rubber [21, 22] or powdered rubber [10] led to an increase in strength.

Test samples show a relatively higher strain as the percentage of crumb rubber aggregates increases [26, 27]

Previous studies have led to different conclusions on the mechanical properties of rubberized concrete and there is no clear margin on the use of waste rubber as a replacement of coarse aggregate [21].

The effect of rubber incorporation on the dynamic properties of concrete has been often of special interest, as a favorable behavior with regard to dynamic loads could be achieved by the elastic material. Of particular importance is the ability of rubberized concrete to dissipate impact energy. It was found that the dynamic modulus of rubberized concrete is lower than that of plain concrete. Moreover, it has been observed that with the increase of rubber content, the damping ratio increased accordingly [27].

The viscous damping ratio was investigated previously [28] using free vibration tests with impact hammer on simply supported beams and drop weight tests. The replacement of up to 20% of sand with rubber resulted in an increase in damping. Beyond 20%, the effect on damping was insignificant. It was concluded that the choice of the rubber content and the mixing process can have a significant effect on the dynamic properties of rubberized concrete.

Partial replacement of fine aggregate with rubber powder was also found to improve the damping properties of concrete [16].

As the weak bond between the rubber and the hardened cement paste was identified as the cause for the impaired mechanical properties of rubberized concrete, the improvement of the bond might be beneficial for the properties of such concrete. Several researchers have investigated different treatments to increase the adhesion of the tire rubber waste aggregate.

Surface modification of crumb rubber by nonionic surfactant (NaOH) was used to achieve more hydrophilic behavior of

the rubber surface. Thus, the interfacial bond between rubber and hardened cement paste was improved [29]. Various other surface treatments of the rubber are reported in literature to improve the interfacial bond, such as soaking in water [30], use of solvents [31], application of oxidizing solutions [32], treatment with alkaline activation and silica fume [33].

As results from previous studies have shown that surface modification of coarse aggregates by silicon, epoxy and sand has the potential to improve the mechanical and dynamic properties of concrete [34].

Therefore, this study investigates the effect of rubber on mechanical and dynamic properties of concrete, especially on its damping behavior. Since the bond between the rubber and the concrete matrix is weak, to improve the interfacial properties of the rubber, a novel coating approach using epoxy and sand is applied.

2. MATERIALS AND METHODS

2.1 Materials

The concrete used in this study consisted of OPC 42.5 grade cement, river sand and crushed stone with a maximum size of 25mm.

Chipped rubber with specific gravity of 1.16 and particle sizes in the range of 20-25 mm were used for the replacement of coarse aggregates. Sika 161- epoxy resin and hardener were obtained from Sika Abyssinia Chemicals Manufacturing PLC.

The physical properties of standard sand, fine and coarse aggregates that were used in the study are presented in Table 1 and the properties of epoxy resin are summarized in Table 2.

Table 1: Physical properties of standard sand, natural sand and coarse aggregates

Material Properties	Standard sand	Sand	Coarse aggregate
Specific gravity	2.62	2.51	2.71
Moisture content %	<0.2	2.41	1.3
Water absorption %	0.79	2.04	1.02

Table 2: Properties of Sika -161 Epoxy resin [35]

Material Properties	Value	Standards
Density	~1600 kg/m ³ at +23 °C	DIN EN ISO 2811-1
Shore D Hardness	~76 (7 days / +23 °C)	DIN 53 505
Tensile Adhesion Strength	> 1.5 N/mm ² (failure in concrete)	ISO 4624
Compressive Strength	> 45 N/mm ² (mortar screed, 28 days / +23 °C / 50 % r.h.)	EN 13892-2

Material Properties	Value	Standards
Tensile Strength in Flexure	~15 N/mm ² (mortar screed, 28 days / +23 °C / 50 % r.h.)	EN 13892-2

The gradation requirement of natural sand and coarse aggregate were checked and both satisfied the requirement set on AASHTO No. T 27 [36] and ASTM C 136 [37] standards.

2.2 Methods

Chipped rubber for replacement of coarse aggregates in normal concrete was prepared by cutting waste tire rubber into small chips. Chipped rubber used in this study is shown in Figure 1. Moreover, Figure 2 shows epoxy and sand coated rubber samples.

To enhance the adhesion of rubber to the concrete mixture, Sika-161 epoxy resin in combination with standard sand 0.75-2.0 mm was used for coating rubber aggregates. Mix ratio (epoxy resin: hardener) of coating materials is 1:0.265.



Figure 1 Chipped rubber samples

In the process of coating the rubber surface, the rubber particles were appropriately cleaned and epoxy resin was applied using hand coating (manual method). After 45-60 min, the epoxy coated rubber was blended with standard sand. The sand coated rubber

was dried for three days at room temperature. During the process, the sand is sticking to the rubber surface.



(a)



(b)

Figure 2(a) Epoxy coated rubber and (b) Sand coated rubber samples

2.2.2 Mix Design

The mix proportion of cement, sand and coarse aggregate was 1:1.5:2.5. The water-cement ratio of 0.45 was used. In developing concrete mixes, all mix design parameters (fine aggregate, cement content,

Damping Properties of Concrete with Sand Coated Rubber Aggregates

w/c ratio) were kept constant except for the coarse aggregate constituents.

Mixture composition of the constituent material for different replacement levels of coarse aggregate is shown in Table 3. Concrete mixtures with replacement of a maximum 25 % coarse aggregate by chipped rubber particles (uncoated or coated) with an

increment of 5% were considered. The control mix was designated as CM-0, concrete with rubber as RA-n, with sand coated rubber as SCRA-n.

The letter n indicates the replacement level (e.g., SCRA-10 represents concrete with 10% replacement of coarse aggregate by sand coated rubber).

Table 3: Mix proportions of concrete with different replacement level

Mix design	Replacement Level					
	0%	5%	10%	15%	20%	25%
Cement (kg)	16.6	16.6	16.6	16.6	16.6	16.6
Sand (kg)	27.7	27.7	27.7	27.7	27.7	27.7
Gravel (kg)	42.7	40.5	38.4	36.3	34.2	31.9
Rubber/ Sand coated (kg)	0.0	2.2	4.3	6.4	8.5	10.8

2.3 Experimental Setups

i) Mechanical Properties

The measured mechanical properties of concrete, included compressive strength, split tensile and flexural strengths. Tests were carried out at 28 days aged

concrete specimens and testing procedures were in accordance with EN Standards. Standards, specimen dimensions for different types of concrete tests are shown in Table 4. The flexural strength test was carried out by a three-point loading test.

Table 4: Standards, specimen dimensions for different types of concrete tests

No.	Test	Standards	Specimen dimensions
1	Compressive strength	EN 12390-4: 2019 [38]	Cube (150 mm)
2	Split tensile strength	EN 12390-6:2009 [39]	Cylinder (300 mm in length and 150 mm in diameter)
3	Flexural strength	EN 12390-5:2009 [40]	Prismatic beam (100 × 100 × 500 mm)

ii) Determination of damping ratio

Damping was utilized to characterize the ability of structures or subsoil to dissipate energy during dynamic response. Damping values depend on several factors, such as:

vibration amplitude, material, mode shape, fundamental periods of vibration, etc. [41].

Damping ratio is the parameter representing the property of materials in vibration reduction. Damping properties are expressed

by the damping ratio (ξ) which can be identified by analyzing the wave using the logarithmic decrement method [42, 43].

To determine the damping ratios of the beam, free vibration was generated by dropping a steel ball (2.0 kg) from a height of 450 mm on a 100 mm×100 mm×500 mm cantilever beam specimen.

The accelerometer (Arduino type, MPU-6050) was set on the free end of the specimen to measure the vibration response. The position of the accelerometer sensor was set at 20 mm from the free end and the free length of the cantilever is 400 mm. Test setups are shown in Figures 3 and 4.

The Arduino UNO board was connected to a computer via Arduino software to record the acceleration amplitudes for the impact tests and then transformed to the frequency domain through Fast Fourier Transform (FFT) using MATLAB code.



Figure 3 Arduino type accelerometer



Figure 4 Test setup for measuring the acceleration of a concrete beam specimen

Damping ratio was determined by using the free vibration decay method of calculating a logarithmic decrement (δ), which is the simplest and most frequently used method through experimental measurements.

The system was excited by performing free oscillations and subsequently, the peak amplitudes over n consecutive cycles were measured [44].

The logarithmic decrement is the natural logarithm of the peak amplitude ratio over n consecutive cycles, that represents damping characteristics and can be determined using the following Eq. (1)[44].

$$\delta_n = \ln\left(\frac{u_i}{u_{i+n}}\right) \quad (1)$$

Where:

u_i and u_{i+n} are peak amplitudes over n consecutive cycles.

The damping ratio can be calculated from logarithmic decrement using Eq. (2),

$$\xi = \frac{\delta_n}{\sqrt{4\pi^2 n^2 + \delta_n^2}} \quad (2)$$

Where:

ξ is a damping ratio (%),

Damping Properties of Concrete with Sand Coated Rubber Aggregates

δ_n is logarithmic decrement

Alternatively, the acceleration amplitudes were recorded for the impact weight tests and the values of the damping ratio were calculated using Eq. (3) [16, 43].

$$\xi = \frac{1}{2n\pi} \ln \left(\frac{A_o}{A_n} \right) \quad (3)$$

Where:

A_o is an initial amplitude

A is the amplitude after n cycles

3. RESULTS AND DISCUSSIONS

3.1 Mechanical Properties

The mechanical properties of concrete with partial replacement of coarse aggregates by chipped rubber and sand coated rubber, including compressive strength, split tensile and flexural strengths are discussed in the following subsections. The results represent the average values of three individual specimens.

3.1.1 Compressive strength of concrete

Figure 5 shows the compression strength of concrete for different concrete mixes. The loading rate was 0.28 MPa/sec.

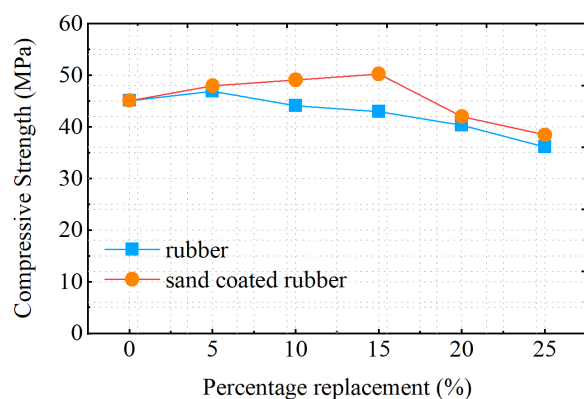


Figure 5 Compressive strength (MPa)

As shown in Figure 5, for the reference mix, a compressive strength of 45.1 MPa was achieved. The concrete could thus be assigned to strength class C30/37. For 5% replacement of coarse aggregate by rubber chips, the compressive strength of concrete was increased, but a further increase beyond this level caused a reduction in compressive strength. Hence, the optimum compressive strengths were found to be 50.3 MPa (SCRA-15) and 47.0 MPa (RA-5). These results indicated an increase in compressive strength of 12.5% and 4.1%, respectively, as compared to the control mix. Concrete with sand coated rubber aggregates gained a higher compressive strength than the uncoated rubber aggregates. This positive effect of epoxy-sand coating is due to the improvement of bond between the rubber surface and the cementitious matrix.

3.1.2 Tensile and Flexural strengths

Test results related to split tensile and flexural strengths are plotted in Figures 6 and 7 respectively.

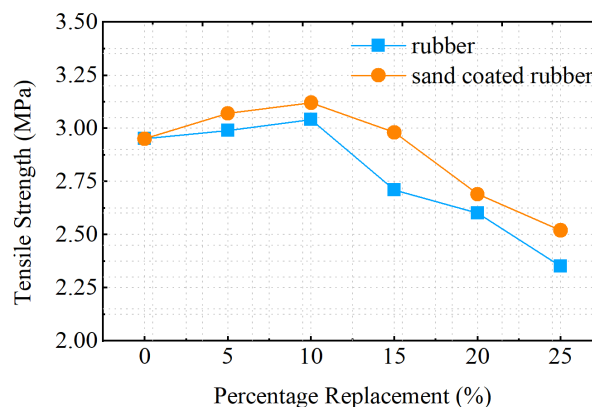


Figure 6 Split tensile strength (MPa)

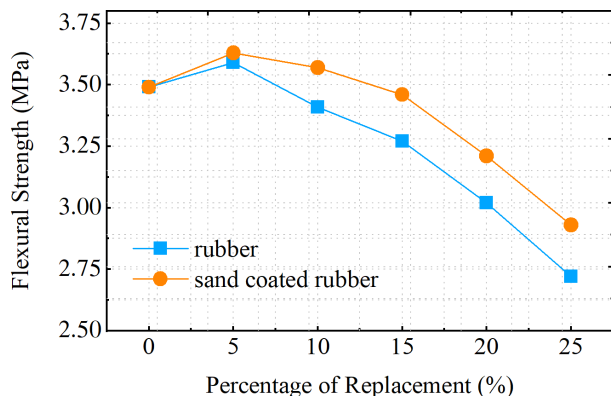


Figure 7 Flexural strength (MPa)

Figures 6 and 7 showed that, for the control mix, split tensile and flexural strengths of 2.9 MPa and 3.5 MPa were achieved, respectively. Moreover, the split tensile strength reached its maximum value at 10% replacement by both rubber and sand coated rubber aggregates. But, beyond the optimum level, reduction in split tensile strength was observed. For both concrete with rubber and sand coated rubber aggregates, a maximum value of flexural strength was observed at a replacement level of 5%.

3.1.3 Damping ratio

An impact test was conducted to determine the damping ratio of concrete specimens based on free vibration responses. Examples of acceleration time history response are shown in Figures 8-10.

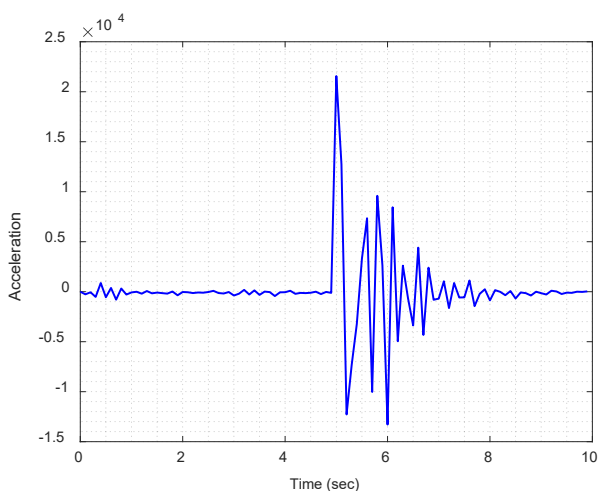


Figure 8 Acceleration time history- CM-0

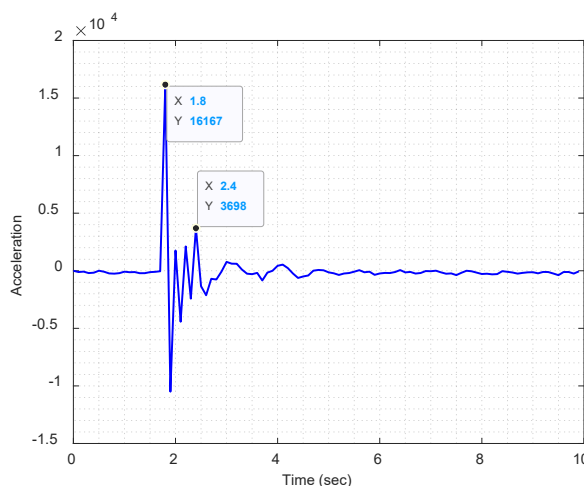


Figure 9 Acceleration time history - RA-25

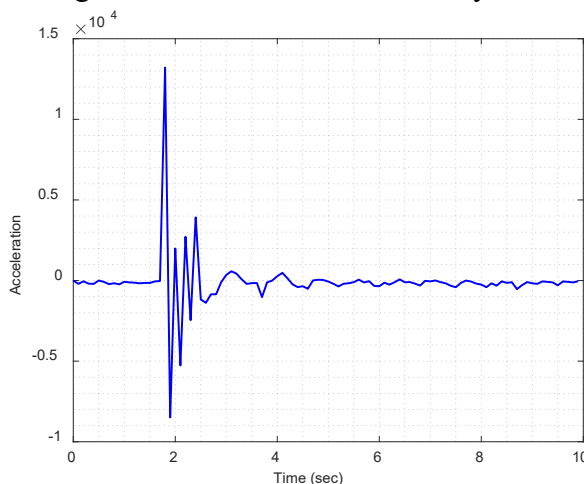


Figure 10 Acceleration time history- SCRA-20

The first and the fourth amplitudes of the vibration response are used to determine the logarithmic decrement and damping ratio. The logarithmic decrement and the damping ratio could be calculated using Eqs.(1) and (3), respectively, and the results are presented in Table 5. Moreover, the damping ratio for concrete with different replacement level of uncoated rubber and sand coated rubber aggregates is shown in Figure 11.

Damping Properties of Concrete with Sand Coated Rubber Aggregates

Table 5: Damping ratio of concrete with rubber and sand coated rubber aggregates

Mix	acceleration amplitudes		acceleration amplitudes in G-forces (g)		δ_n	Damping ratio (%)
	y1	y4	y1	y4		
CM-0	21569	8442	1.316	0.515	0.938	4.95
RA-5	14636	5139	0.893	0.314	1.047	5.54
RA -10	11478	3801	0.701	0.232	1.105	5.86
RA -15	16822	4717	1.027	0.288	1.272	6.73
RA -20	15171	3895	0.926	0.238	1.360	7.20
RA -25	16167	3698	0.987	0.226	1.475	7.81
SCRA -5	13808	5093	0.843	0.311	0.997	5.27
SCRA -10	12707	4527	0.776	0.276	1.032	5.47
SCRA -15	12643	3998	0.772	0.244	1.151	6.10
SCRA -20	13207	3917	0.806	0.239	1.215	6.44
SCRA -25	12462	3961	0.761	0.242	1.146	6.09

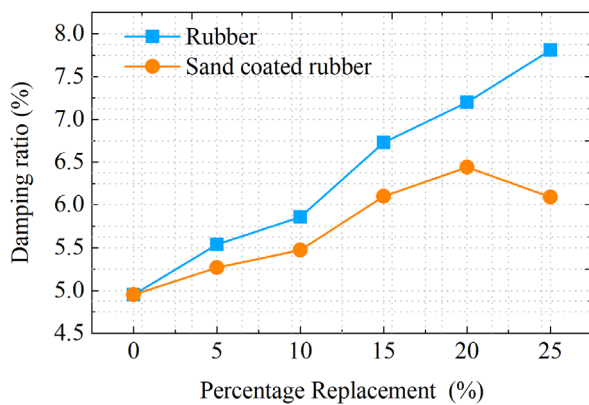


Figure 11 Damping ratio of rubber and sand coated rubber aggregates

From Figure 11, it can be observed that, the damping ratio increases with increasing percentage of chipped tire rubber content. It was also observed that, the damping ratio

increases with an increase in percentage of sand coated rubber aggregates reaches up to 20%. As the percentage of sand coated rubber content increases from 20% to 25%, the damping ratio started to decline. However, the value was higher than that of the control mix, which is an increment of 23%.

3.2 Comparative Study

In this section, test results of this study are compared with previous studies. The comparisons are summarized in Tables 6-8. These comparisons consider only results of compressive strength, flexural strength and damping ratio of concrete with partial replacement of coarse aggregates by uncoated rubber chips.

Table 6: Comparison of compressive strength

Replacement level (%)	Study by Sofi, A. [14]		Study by Vijayan, D. S., kumar, et al. [25]		Study by Sibiyone, K. Paul, and M. L. Sundar [21]		Study by Paparao, A., et al. [22]		This study	
	Compressive strength (MPa)	Increment (%)	Compressive strength (MPa)	Increment (%)	Compressive strength (MPa)	Increment (%)	Compressive strength (MPa)	Increment (%)	Compressive strength (MPa)	Increment (%)
0	32.00	-	37.11	-	24.90	-	25.00	-	45.12	-
5	33.50	4.69	32.53	-12.34	27.50	10.44	27.20	8.80	46.95	4.06
10	25.00	-21.88	28.93	-22.04	29.33	17.79	29.30	17.20	44.15	-2.15
15			21.05	-43.27	29.20	17.27	26.60	6.40	42.98	-4.74
20			16.87	-54.54	28.89	16.02	28.89	15.56	40.38	-10.51
25					28.50	14.46	25.33	1.32	36.09	-20.01

Table 7: Comparison of flexural strength

Replacement level (%)	Study by Sofi, A. [14]		Study by Vijayan, D. S., kumar, et al. [25]		Study by Sibiyone, K. Paul, and M. L. Sundar [21]		Study by Paparao, A., et al. [22]		This study	
	Flexural strength (MPa)	Increment (%)	Flexural strength (MPa)	Increment (%)	Flexural strength (MPa)	Increment (%)	Flexural strength (MPa)	Increment (%)	Flexural strength (MPa)	Increment (%)
0	5.25		11.75	-	3.10	-	3.20	-	3.49	-
5	5.20	-0.95	12.04	2.08	3.53	13.87	3.50	9.37	3.59	2.87
10	3.30	-37.14	11.50	-2.13	3.80	22.58	3.90	21.88	3.41	-2.29
15			8.25	-29.79	3.71	19.35	3.62	13.13	3.27	-6.30
20			6.50	-44.68	3.50	12.90	3.40	6.25	3.02	-13.47
25					3.45	11.29	3.30	3.13	2.72	-22.06

Table 8: Comparison of damping ratio

Replacement level (%)	Study by Ching Y., George C., et. al. [16]		Study by L. Zheng, X. Sharon Huo, et. al. [27]		Study by Maru Sete [8]		This study	
	Damping Ratio(%)	Increment (%)	Damping Ratio(%)	Increment (%)	Damping Ratio(%)	Increment (%)	Damping Ratio(%)	Increment (%)
0	1.0	-	0.74	-	6.93	-	4.95	-
5	1.25	25	0.98	32.43	8.34	20.35	5.54	11.92
10			1.19	60.81	8.16	17.75	5.86	18.38
15			1.38	86.49	16.17	133.33	6.73	35.96
20					16.52	138.38	7.20	45.45
25					22.83	229.44	7.81	57.78

As shown in Table 6, a study by Sofi, A. [14], showed that the compressive strength of concrete increased by 4.69% when 5% rubber chips were used. Beyond this level, the strength decreased. The trend of the results is similar to our study. However, the results by Vijayan, D. S., Kumar, et al. [25] showed that the presence of rubber contents in concrete mixes has a negative effect and there is a very considerable loss in compressive strength observed.

On the other hand, according to Sibiyone, K. Paul, and M. Lenin Sundar [21] and study by Paparao, A., et al. [22], test results of compressive and flexural strength increased with increasing percentage of rubber content in concrete ranging from 0% to 40%.

Moreover, the study by Vijayan, D. S., et al. [25], shown in Table 7 indicates, an increment of 2.08% in flexural strength was observed when 5% rubber is used and gradual decrement in flexural strength was noticed as the percentage of rubber increased. The trend of the results is similar to that of this study.

From Table 8, the study by Ching Y., George C. et. al., [16], L. Zheng, X. Sharon,

et. al. [27] and Maru Sete [8], indicated that the damping ratio increases as the rubber content in concrete mix increases. However, the increment is much higher than as compared to this study.

In general, except for those studies reported by Sibiyone, K. Paul, [21] and Paparao, A., et al., [22], this study shows similar trends (strength reduction, improvement in damping ratio) to previous studies when the natural coarse aggregates are partially replaced by rubber chips. However, the findings of this study are different from other similar studies conducted by [21] and [22] due to the following reasons; i) Sibiyone, K. Paul, [21] used admixtures for concrete mix design as well as scrap rubber with a size of less than 10 mm in their studies, ii) in the case of a study conducted by Paparao, A., M. Aruntej, [22] scrap rubber with a size of 10-12 mm was used.

4. CONCLUSIONS

In this study, the mechanical properties and damping capacity of concrete with various percentage replacement of coarse aggregates by rubber and epoxy-sand coated rubber up

to 25%, were experimentally studied. The results revealed that when 5% uncoated rubber and 15% epoxy-sand coated rubber aggregates are used, the compressive strength of concrete is optimal. Beyond the optimum replacement levels, reduction in compressive, splitting tensile and flexural strength was noticed as compared to the reference mix.

The partial replacement of coarse aggregates with rubber and epoxy-sand coated rubber improves the damping ratio of concrete. A maximum of 58% increase in damping ratio was reached for the uncoated rubber, while a 23% increase was reached for epoxy-sand coated rubber aggregates. The epoxy-sand coating thus can mitigate the negative effect of the rubber on the mechanical properties to some extent. However, that effect is to the detriment of the improvement of the damping behavior by the rubber.

Waste tire rubber can be used as an alternative source of construction material to replace the natural coarse aggregate in concrete. Hence, it is recommended to use epoxy and sand to coat the rubber in order to enhance the bonding between the rubber surface and the mortar. Moreover, in order to improve the energy dissipation (damping ratio) of concrete, it is recommended to replace the natural aggregate by rubber and epoxy-sand coated rubber chips.

CONFLICT OF INTEREST

The authors declare that there is no conflict of interest.

ACKNOWLEDGEMENTS

Tests were conducted in "Addis Ababa University, Addis Ababa Institute of Technology (AAiT), School of Civil and Environmental Engineering, Materials Testing Laboratory", which is highly acknowledged by the authors.

REFERENCES

- [1] Thomas, B. S., & Gupta, R. C., "*A Comprehensive Review on the Applications of Waste Tire Rubber in Cement Concrete*", *Renewable and Sustainable Energy Reviews*, Vol. 54, 2016, pp. 1323-1333.
- [2] Mashiri, M. S., Vinod, J. S., Sheikh, M. N., & Tsang, H. H., "*Shear Strength and Dilatancy Behavior of Sand-Tyre Chip Mixtures*", *Soils and Foundations*, Vol. 55, No. 3, 2015, pp. 517-528.
- [3] Raffoul, S., Garcia, R., Pilakoutas, K., Guadagnini, M., & Medina, N. F., "*Optimization of Rubberized Concrete with High Rubber Content: An Experimental Investigation*", *Construction and Building Materials*, Vol. 124, 2016, pp. 391-404.
- [4] Conesa, J. A., Martín-Gullón, I., Font, R., & Jauhiainen, J. J. E. S., "*Complete Study of the Pyrolysis and Gasification of Scrap Tires in a Pilot Plant Reactor*", *Environmental Science & Technology*, Vol. 38, No. 11, 2004, pp. 3189-3194.
- [5] Tesfaye Gebrehanna, "*Organizational Performance and Challenges of Tyre Manufacturing in Ethiopia: The case of Horizon Addis Tyre Factory*", MA. Thesis, St. Mary's University, 2018.
- [6] Yimreha Mekonnen, "*Evaluation of Financial Forecasting Method of Horizon Addis Tyre Share Company*", MA. Thesis, St. Mary's University, 2013.
- [7] Misgana Berhanu, "*Study on Shear Strength of Concrete Mixed with Waste Tires Steel Wire*", MSc. Thesis, AAiT, Addis Ababa, Ethiopia, March, 2020.
- [8] Maru Sete, "*Mechanical and Dynamic Properties of Rubberized Concrete*",

Damping Properties of Concrete with Sand Coated Rubber Aggregates

- Addis Ababa Institute of Technology, MSc Thesis, AAiT, Addis Ababa, Ethiopia, March, 2021.
- [9] Ganjian, E., Khorami, M., and Maghsoudi, A., "*Scrap-Tyre-Rubber Replacement for Aggregate and Filler in Concrete*", *Construction and Building Materials*, Vol. 23, No. 5, 2009, pp. 1828-1836.
- [10] Gerges, N. N., Issa, C. A., & Fawaz, S. A., "*Rubber Concrete: Mechanical and Dynamical Properties*", *Case Studies in Construction Materials*, Vol. 9, 2018, pp. e00184.
- [11] Henry, M., Yamashita, H., Nishimura, T., & Kato, Y., "*Properties and Mechanical-Environmental Efficiency of Concrete Combining Recycled Rubber with Waste Materials*", *International Journal of Sustainable Engineering*, Vol. 5, No.1, 2012, pp. 66-75.
- [12] Mushunje, K., Otieno, M., & Ballim, Y., "*Partial Replacement of Conventional Fine Aggregate with Crumb Tyre Rubber in Structural Concrete - Effect of Particle Size on Compressive Strength and Time Dependent Deformations*", *MATEC Web of Conferences*, EDP Sciences, Vol. 199, 2018, pp. 11002.
- [13] Stergios Mitoulis, A.R. Bennett, "*Effect of Waste Tire Rubber Additive on Concrete Mixture Strength*", *British Journal of Environmental Sciences*, Vol. 4, No. 4, 2016, pp. 11-18.
- [14] Sofi, A. "*Effect of Waste Tyre Rubber on Mechanical and Durability Properties of Concrete*", *Ain Shams Engineering Journal*, Vol. 9, No. 4, 2018, pp. 2691-2700.
- [15] Almaleeh, A. M., Shitote, S. M., & Nyomboi, T., "*Use of Waste Rubber Tyres as Aggregate in Concrete*", *Journal of Civil Engineering and Construction Technology*, Vol. 8, No. 2, 2017, pp. 11-19.
- [16] Lin, Ching-Yao, George C. Yao, and Chung-Hong Lin. "*A Study on the Damping Ratio of Rubber Concrete*", *Journal of Asian Architecture and Building Engineering*, Vol. 9, No. 2, 2010, pp. 423-429
- [17] Parmar, A., Joshi, C., Parmar, A., Patel, U., & Vaghasiya, A. "*Use of Crumb Rubber as a Partial Replacement of Coarse Aggregate in Conventional Concrete*", In *Proceeding of 3rd Afro-Asian International Conference on Science, Engineering & Technology AAICSET*, 2015.
- [18] Thiruppathi, R. "*Discarded Tyre Rubber as Concrete Aggregate: A Possible Outlet for Used Tyres*", *International Conference on Current Trends in Engineering and Technology (ICCTET)*, IEEE, 2013, pp. 202-207.
- [19] Toutanji, H. A., "*The use of Rubber Tire Particles in Concrete to Replace Mineral Aggregates*", *Cement and Concrete Composites*, Vol. 18, No. 2, 1996, pp. 135-139.
- [20] Liu, F., Zheng, W., Li, L., Feng, W., & Ning, G. "*Mechanical and Fatigue Performance of Rubber Concrete*", *Construction and Building Materials*, Vol. 47, 2013, pp. 711-719.
- [21] Sibiyone, K. Paul, and M. Lenin Sundar, "*Experimental Study on Replacing Waste Rubber as Coarse Aggregate*", *International Journal of ChemTech Research* Vol. 10, No. 14, 2017, pp. 287-293

- [22] Pappas, A., M. Aruntej, and Y. Sombabu, "An Experimental Study on Partial Replacement of Coarse Aggregate by Waste Rubber", *International Journal for Recent Development in Science and Technology*, Vol. 04, No. 6, 2020, pp. 215-218
- [23] Khaloo, A. R., Dehestani, M., & Rahmatabadi, P., "Mechanical Properties of Concrete Containing a High Volume of Tire-Rubber Particles", *Waste Management*, Vol. 28, No. 12, 2008, pp. 2472–2482.
- [24] Khatib, Z. K.; Bayomy, F. M, "Rubberized Portland Cement Concrete", *Journal of Materials in Civil Engineering*, Vol. 11, No. 3, 1999, pp. 206-213.
- [25] Vijayan, D.S., Dinesh kumar, Mohammed Aamir K.N, Muhammed Shahim P.A, and Gokul Balagopal, "Experimental Investigation on Partial Replacement of Coarse Aggregate with Shredded Rubber in Concrete", *International Journal of Advanced Science and Technology* Vol. 29, No.7, 2020, pp. 2411-2423.
- [26] Abaza, O. A., & Shtayeh, S. M., "Crumbed Rubber for Non-structural Portland Cement Concrete Applications", *Dirasat, Engineering Science*, Vol. 37, No. 2, 2010, pp. 214-225.
- [27] Zheng, L., Huo, X. S., & Yuan, Y., "Experimental Investigation on Dynamic Properties of Rubberized Concrete", *Construction Building Materials*, Vol. 22, No. 5, 2008, pp. 939-947.
- [28] Moustafa, A., & ElGawady, M. A, "Dynamic Properties of High Strength Rubberized Concrete", *ACI Spec. 314*, 2017, pp. 1-22.
- [29] Jamnongwong, M., & Sukontasukkul, P. "Use of Surfactant to Improve Properties of Crumb Rubbers in Concrete Products", *Rheology and Processing of Construction Materials, RheoCon2 & SCC9 2*, Springer International Publishing, 2020, pp. 27-35.
- [30] Mohammadi, I., Khabbaz, H., & Vessalas, K., "In-depth Assessment of Crumb Rubber Concrete (CRC) Prepared by Water-Soaking Treatment Method for Rigid Pavements", *Construction and Building Materials*, Vol. 71, 2014, pp. 456-471.
- [31] Rivas-Vázquez, L. P., Suárez-Orduña, R., Hernández-Torres, J., & Aquino-Bolaños, E., "Effect of the Surface Treatment of Recycled Rubber on the Mechanical Strength of Composite Concrete/Rubber", *Materials and Structures*, Vol. 48, 2015, pp. 2809-2814.
- [32] Khern, Y. C., Paul, S. C., Kong, S. Y., Babafemi, A. J., Anggraini, V., Miah, M. J., & Šavija, B., "Impact of Chemically Treated Waste Rubber Tire Aggregates on Mechanical, Durability and Thermal Properties of Concrete", *Frontiers in Materials*, Vol. 7, 2020, pp. 1-11.
- [33] Pelisser, F., Zavarise, N., Longo, T. A., & Bernardin, A. M., "Concrete made with Recycled Tire Rubber: Effect of Alkaline Activation and Silica Fume Addition", *Journal of cleaner production*, Vol. 19, No. 6-7, 2011, pp. 757-763.
- [34] Yisihak Gebre, Tom Lahmer, Matthias Müller, Torben Wiegand, Andrea Osburg and Abraham Gebre,

Damping Properties of Concrete with Sand Coated Rubber Aggregates

- "Properties of Concrete with Coated Aggregates Under Different Loading Conditions"*, Journal of Research in Engineering and Applied Sciences (JREAS): Vol. 8, No. 01, 2023, pp. 449-459.
- [35] Sikafloor®-161, Product Data Sheet, May 2019.
- [36] AASHTO No. T 27, "*Standard Method of Test for Sieve Analysis of Fine and Coarse Aggregates*", 2014.
- [37] ASTM C 136, "*Standard Test Method for Sieve Analysis of Fine and Coarse Aggregates*", 2014.
- [38] EN 12390-4:2019, "*Testing Hardened Concrete Part 4: Compressive Strength*", 2019.
- [39] EN 12390-6:2009, "*Testing Hardened Concrete - Part 6: Tensile Splitting Strength of Test Specimens*", 2009.
- [40] EN 12390-5:2009, "*Testing Hardened Concrete - Part 5: Flexural Strength of Test Specimens*", 2009
- [41] Bachmann, H., Ammann, W. J., Deischl, F., Eisenmann, and J., Floegl, I., "*Vibration Problems in Structures Practical Guidelines*", Springer Science & Business Media, 1995.
- [42] Faizah, R., & Aminullah, A., "*Simple Laboratory Test to Measure Damping Properties of Hardened Mortar or Concrete Elements*", International Journal of Sustainable Construction Engineering and Tech., Vol. 11, No. 01, 2020, pp. 76-86.
- [43] Yan, L., Jenkins, C. H., & Pendleton, R. L., "*Polyolefin Fiber-Reinforced Concrete Composites Part I. Damping and Frequency Characteristics*", Cement and concrete research, Vol. 30, No. 3, 2000, pp. 391-401.
- [44] Gabryś, K., Soból, E., Sas, W., and Szymański, A, "*Material Damping Ratio from Free-Vibration Method* ", Annals of Warsaw University of Life Sciences - SGGW Land Reclamation, Vol. 50, No. 2, 2018, pp. 83-97.

Fault Tolerant Digital Controller for DC-DC Switching Power Converter Using Modular Redundancy

Daniel Dilbie, Getachew Alemu

School of Electrical and Computer Engineering, Addis Ababa Institute of Technology (AAiT),
Addis Ababa University (AAU)

Corresponding author's Email: *daniel@aait.edu.et*

ABSTRACT

Power converters and regulators are the main and critical building blocks of all electronic systems. In applications prone to transient faults, such as particle strikes, spatial redundancy techniques can improve the reliability significantly. The design of a fully digital DC/DC switching buck converter regulator based on a fault tolerant modular redundancy architecture implemented on SRAM FPGAs is presented. Transient events such as single event functional interrupts (SEFIs) are the dominant effects in SRAM-based FPGAs. SEFIs result in missing pulses in the generated PWM control signal of the converter that cause large transient drops at the converter output. In this work, triple modular redundancy (TMR) technique is used to implement spatial redundancy. This approach is used to triplicate the physical digital blocks on FPGA such that faults on one of the modules can be detected and corrected while the system works uninterrupted and with correct output. Experimental results indicate that with triple modular redundancy, the power converter can withstand up to 5x more doze of faults as compared to conventional power converters.

Keywords: *single event functional interrupt (SEFI), Fault tolerant design, spatial*

redundancy, DC/DC switching power converter, buck converter, digital control.

I. INTRODUCTION

DC/DC switching power converters, due to their high-efficiency conversion, are essential parts of modern electronic systems [1], [2]. The main objective of this work is to design a fault tolerant FPGA-based digital control system for a DC-DC buck converter/regulator. Digital control systems have significant advantages over conventional analog pulse width modulators (PWMs) [3], [4].

Along with the general advantages of a digital system (such as high flexibility, reduced sensitivity to noise and component parameter variations, and the capability to realize sophisticated control algorithms), a digital controller can be hardened more easily against transient faults than its analog counterpart. In fact, a conventional PWM switching converter is very susceptible to single-event effects (SEEs) in the error amplifier stage and in the analog PWM controller that cause large transient pulses at its output [5]-[7]. The use of commercial SRAM-based FPGAs in applications such as solar power converters in satellites is very attractive because of their high component density, quick turn-around time, and reconfigurability [7], [9].

Normally, SRAM-based FPGAs are very sensitive to SEEs. The dominant effect is the single event functional interrupt (SEFI) caused by a configuration memory bit upset that disrupts the continuous operation of the system in which the FPGA is used. Heavy ion radiation testing on these devices has shown that no permanent faults occur after an SEFI, and that reprogramming the FPGA will restore full functionality [10], [11]. Therefore, “radiation hardening by design” (RHBD) techniques based on detecting, mitigating and correcting SEFIs make it possible to use SRAM-based FPGAs in high radiation environments [12].

The paper is organized as follows. Section II describes the design of a digitally controlled switching buck converter. In Section III the main radiation effects on SRAM FPGAs are discussed and the technique applied to harden the design against radiation-induced errors is illustrated. Section IV shows the simulated and experimental results, and section V concludes and summarizes the work.

II. DIGITALLY CONTROLLED BUCK CONVERTER

A DC/DC switching buck converter steps down an unregulated input voltage, such as from a solar panel, to a regulated output voltage for a wide range of input voltages and load conditions. The circuit uses an inductor, a power MOSFET to transfer power from the input to the output in an efficient way, a capacitor to smooth out the ripple in the output, and a freewheeling diode (or a MOSFET synchronous rectifier for highest efficiency). The MOSFET is periodically switched from the on state to the off state and vice versa. The ratio between the on-state time interval and the switching period (duty cycle) determines the DC value of the output voltage. To maintain the required

output voltage in the presence of variations in the input voltage and load conditions, a feedback network, which controls the duty cycle, is used [1].

Figure 1 shows the basic structure of a digitally controlled DC/DC switching buck converter in which the feedback loop is implemented using an analog-to-digital converter(ADC). The actual output voltage V_o is scaled by the sensor gain and converted into a digital signal by means of a sampling process and analog-to-digital conversion (ADC). The difference between the digitized sample of the converter output and the reference voltage (Ref) forms an error signal e that is processed by the digital compensator to calculate the actual duty cycle c . The digital pulse width modulator (PWM) generates the switching signals (H and L) that control the two power MOSFETs.

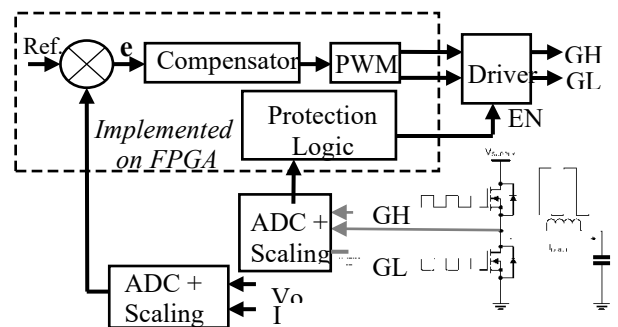


Fig. 1. Basic schematic of a digitally controlled buck converter.

In this work, triple modular redundancy (TMR) technique is used to implement spatial redundancy as shown in Figure 2. This approach is used to triplicate the physical digital blocks on FPGA such that faults on one of the modules can be detected and corrected while the system works uninterrupted and with correct output. The classic three voter configuration provides the best reliability compared to all other

configurations [13]. The drawback of the classic three voter is that it takes the largest space in hardware implementations. However, for small circuits, such as this particular application, space is not a constraint. Therefore, it is justified to choose the classic three voter configuration to achieve the best reliability.[14].The reference (Ref) is continuously compared with the feedback signal (FB). The error signal from the comparator is passed to the proportional and integral (P) compensator. The compensators output is then used to set the duty cycle of the Pulse with modulator (PW). The majority voter logic (V) takes the correct majority of the the three parallel outputs at each stage and the PWM check logic makes sure the integrity of the pulse output.

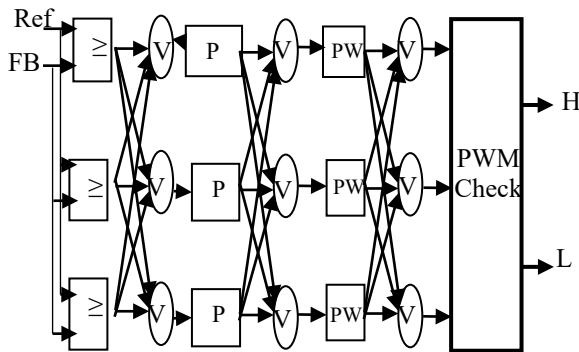


Fig. 2. Block diagram of the designed TMR controller.

III. SINGLE EVENT EFFECTS ON SRAM FPGAS AND FAULT TOLERANT DESIGN

Heavy ion testing on SRAM FPGAs from different semiconductor manufactures has shown that these parts are very sensitive to radiation-induced errors [9]-[11]. The dominant error is the single event functional interrupt, which is caused by a configuration memory bit flip. It is worth noting that a user flip-flop is as susceptible as a configuration memory cell to radiation-

induced upset. However, the number of configuration bits is much greater than that of the user flip-flops and thus the probability of an SEFI is significantly greater than the probability of an SEU (single event upset) associated with a user register. Moreover, no permanent faults, such as single event latch-up or dielectric rupture, have been observed during heavy ion tests. In addition, reprogramming the FPGA will restore the full functionality of the device, after the occurrence of an SEFI. Therefore, RHBD techniques based on detecting, mitigating and correcting SEFIs make it possible to use SRAM FPGAs in high radiation environments [12], [13].

When applying a digital control signal using an SRAM-based FPGA in a switching converter, radiation induced SEFIs result in missing pulses in the generated PWM control signal of the converter. In turn, the missing pulses result in large transient voltage drops at the output of the converter that may adversely affect the operation of the powered systems [5],[6]. Therefore, an RHBD technique must be applied to mitigate and correct the SEFIs. In the work described here, a redundant approach at both the logic design and the device levels has been applied.

IV. EXPERIMENTAL RESULTS

In order to validate this approach a TMR digital circuit was implemented on Xilinx Zynq-7000 SoC. This SoC integrates Xilinx Artix-7 FPGA and a dual core ARM cortex-A9 MPU on a single chip. The TMR architecture in Fig 2 is implemented on the FPGA while the Cortex-A9 is used to simulate single event effects on the FPGA configuration memory. Table 1 below summarizes the FPGA resources used for conventional controller design and for TMR implementation with triplicated voters.

Table 1 Comparison between standard and TMR designs in Artix-7 XC7A200T

Digital DC-DC controller design on SRAM FPGA	Area (# slices)	# Logic cells (LC)	# CLB Flip-flops
Total FPGA resources	33,650	215,360	269,200
Standard: No TMR used	9	128	12
Percentage used	0.027 %	0.059 %	0.004 %
FullTMR implementation	21	402	41
Percentage used	0.062 %	0.187 %	0.015 %

According to data from Xilinx datasheet [15], The cost per logic cells (LCs) on the Artix-7 series FPGA is roughly linear at USD 0.0018. The total cost of implementing a standard controller on FPGA has insignificant hardware cost at only 0.06% of LCs used. Also, the TMR version, even if it requires 3x more resources it's still less than 0.19% of the FPGA resource while providing 5x more reliability than the standard controller.

The implementation takes a typical voltage mode control loop designed to give out a regulated 5V output from an unregulated input of 12 – 24V DC (typical solar panel voltage ranges). First, the output voltage is sensed, scaled down and fed to an analog to digital converter which feedback the digital equivalent of the output voltage to the control loop. Then, the feedback is subtracted from a fixed reference to get the error signal. The error signal is passed through the PID compensator to get the control value. The control value determines the pulse width of the next control cycle.

The difference equation was implemented in a control loop with a bandwidth of 50KHz.

$$U(k) = U(k - 1) + K_p \times error + K_i \times Integral + K_d \times \quad (1)$$

Where,

$U(k)$ = current control value,

$U(k - 1)$ = previous control value,

$error(k)$ = current error,

$error(k - 1)$ = previous error,

K_p = Proportional constant,

K_i = Integral constant,

K_D = Derivative constant

The process is broken down to three modules; The comparator module, the PID module and the PWM generator module. The three modules are triplicated to compute the outputs and compare with each other. The error, the control and the pulse width are the three values to be voted on in TMR.

At steady state, with no fault, the duty cycle of the output square wave is constant for a fixed load and constant input. In this particular case, at no load and 12V constant input, the duty cycle is 42% 53% for half load of 2.5W and 65% at a full load of 5W.

Fault Impact Analysis

Fault impact analysis is done by observing the duty cycle of the output pulse from the PWM generator at fixed load conditions. For this test, the load and input voltages are kept constant to observe only the impact of transient faults on the output. The period of the output square wave is kept constant at 1ms (1KHz PWM frequency) and the duty cycle is varied by the controller to keep the output voltage regulated at $5V \pm 1\%$. A momentary fault in the controller will result in a wrong duty cycle of the pulse which may cause a temporary output overshoot or undershoot.

Baseline case

This case is used as a reference. In this case, the system runs without TMR and with no fault injected. The test was run for 10,000 PWM cycles (10 seconds) at steady state and the following result was obtained.

Table 2 Baseline case

Parameters	No load	2.5W load	5W load
Maximum duty cycle	438µs (43.8%)	542µs (54.2%)	670µs (67%)
Minimum duty cycle	412µs (41.2%)	510µs (51%)	645µs (64.5%)
Duty cycle standard deviation	11µs	13µs	19µs
%deviation	2.6%	2.7%	2.9%
Maximum output voltage	5.06V	5.07V	5.08V
Minimum output voltage	4.98V	4.97V	4.95V
Output standard deviation	0.04V	0.04V	0.05V
%deviation	0.8%	0.82%	1%

Result at injection rate of 1/3000 (one in 3000 cycles)

As in the previous case, the test was run for 10,000 pulse cycles (10 seconds) at steady state. Both overshoot and undershoot conditions were observed in the data (even if it is too fast to observe on the scope). Although, the output regulation is not affected as much, the transient could damage the power switches at higher load currents if occurs frequently.

Table 3 Output parameter at fault rate of 1/3000

Parameters	No load	2.5W load	5W load
Maximum duty cycle	820µs (82%)	861µs (86.1%)	924µs (92.4%)

Minimum duty cycle	12µs (1.2%)	28µs (2.8%)	46µs (4.6%)
Duty cycle standard deviation	21µs	26µs	31µs
%deviation	5%	4.9%	4.8%
Maximum output voltage	6.88V	5.87V	5.98V
Minimum output voltage	3.78V	3.86V	3.21V
Output standard deviation	0.09V	0.05V	0.07V
%deviation	1.8%	1.2%	1.4%

Higher fault rates

The following results were obtained at different fault injection rates for 2.5W and 5W load. It is observed that at injection rates lower than (1/1000), the controller loses stability and the output voltage starts to oscillate in both cases.

Table 4 Output parameters at higher fault rates (2.5W/5W loads)

Fault injection rate	Duty cycle deviation (%)	Output voltage deviation (%)
1/5000	2.8/3.1	0.86/1.0
1/2000	8.3/11.2	2.1/2.8
1/1000	21/28.4	8.1/8.7
1/500	40.2/48.9	18.4/21.5

Results with proposed TMR architecture

With TMR, the tests were run again with the same conditions. For the case with no faults injected, the result was identical with the baseline case.

Result at injection rate of 1/3000

No overshoot and undershoot conditions were observed and the result was fairly the same as in the case of no faults.

Table 5 Output parameters with TMR and fault rate of 1/3000

Parameters	No load	2.5W load	5W load
Maximum duty cycle	441 μ s (44.1%)	541 μ s (54.1%)	673 μ s (67.3%)
Maximum output voltage	5.07V	5.07V	5.08V
Minimum output voltage	4.98V	4.96V	4.93V
Output standard deviation	0.044V	0.046V	0.052V
%deviation	0.88%	0.9%	1.04%

Result at higher fault rates

The following results were obtained at different fault injection rates for 2.5W and 5W loads. The controller is observed to be fairly stable at up to injection rates of 1/100. For both load cases, overshoot and undershoot conditions are observed starting from injection rates of 1/200.

Table 6 Output parameters with TMR for higher fault rates (2.5W/5W loads)

Fault injection rate	Duty cycle deviation (%)	Output voltage deviation (%)
1/2000	2.75/3.2	0.98/1.05
1/1000	3.8/4.3	1.02/1.18
1/500	6.1/6.8	1.41/1.82
1/200	12/12.3	2.1/2.8
1/100	20.9/21.2	5.77/6.1

V. CONCLUSION

Power converters and regulators are the main and critical building blocks of all electronic systems. In applications prone to transient faults, such as particle strikes, spatial and time redundancy techniques can improve the reliability significantly.

Minimum duty cycle	410 μ s (41%)	528 μ s (52.8%)	642 μ s (64.2%)
Duty cycle standard deviation	11.3 μ s	15 μ s	20.2 μ s
%deviation	2.69%	2.77%	3.1%

Single event functional interrupts are the dominant radiation effects in SRAM-based FPGAs. This work demonstrates the design of an SEFI-resistant DC/DC switching power converter based on a reconfigurable digital control loop implemented in SRAM FPGAs.

In this project, the results indicate that with classic triple modular redundancy, the power converter can withstand up to 5x more doze of faults as compared to conventional power converters. The additional 3x more hardware requirement is justified because the implementation only used less than 0.2% of the total resource. For such a small circuit the benefits of 5x more reliability very much outweighs the additional hardware cost.

REFERENCES

- [1] S. Cuk, R. D. Middlebrook, "Basics of Switched-Mode Power Conversion: Topologies, Magnetics, and Control," in *Advances in Switching Mode Power Conversion*. Pasadena, CA:TESAco, 1981, vol. 2.
- [2] A. Capel, D. O'Sullivan, J. C. Marpinard, "High-Power Conditioning for Space Applications," *Proc. of the IEEE*, vol. 76, no. 4, pp. 391-408, Apr. 1998.
- [3] T. W. Martin, S. S. Ang, "Digital Control for Switching Converters," *Proc. of IEEE Int. Symp. on Industrial Electronics, ISIE'95*, vol. 2, pp. 480-484, July 1995.
- [4] A. P. Dancy, R. Amirtharajah, A. P. Chandrakasan, "High-efficiency

- Multiple-output DC-DC Conversion for Low-voltage Systems,” IEEE Trans. on VLSI. Systems, vol. 8, no. 3, pp. 252-263, Jun. 2000.
- [5] Ribeiro E, Marques Cardoso AJ, Boccaletti C. “Fault Tolerant Strategy for a Photovoltaic DC-DC Converter.” IEEE Trans. on power Electronics, July 2013.
- [6] Dikshant Khanke, “Design and Implementation of High Reliability PWM Modulator Using TMR with spare arrangement”, IJSR vol 3, issue 7 pp 1595-1597, 2014
- [7] Mamatha S., et al “FPGA Based Digital Controller for DC-DC Buck Converter”, IJIRCCE, May 2015,
- [8] Miro Milanovic, Mitja Truntic, “FPGA Implementation of Digital Controller for DC-DC Buck Converter”, IEEE IDEAS’05
- [10] Felix Siegle, et al, “Mitigation of Radiation Effects in SRAM Based FPGAs for Space Applications”, ACM inc. 2014.
- [11] Masashi Hamamatsu, Tatsuhiro Tsuchiya, “On the Reliability of Cascaded TMR Systems”, the 2010 Pacific Rim International Symposium on Dependable Computing.
- [9] Adam M. Jacobs, “Reconfigurable Fault Tolerance for Space Systems”, PhD dissertation, University of Florida, 2013
- [12] “Radiation Effects and Soft Errors in IC and Electronics Devices”, World Scientific Ltd, 2004
- [13] N. Jing et al, “SEU Fault Evaluation and Characteristics for SRAM Based FPGA Architectures and Synthesis Algorithms”, ACM transaction on Design Automation of Electronic Systems. Vol 18, No 1, 2012.
- [14] Sungjae Lee, Jae-il Jung, “Voting Structure for TMR modules” Electronic Express, Vol 4, No 21
- [15] <https://www.xilinx.com/products/silicon-devices/fpga/artix-7.html> (accessed: July 23, 2022)

MODELING AND SIMULATION OF A MICRO-HYDROPOWER SYSTEM FOR RURAL ELECTRIFICATION (A CASE STUDY OF TEMECHA RIVER, AMHARA REGION, ETHIOPIA)

Getnet Belie Endalie ^{a*}, Tilahun Nigussie Gemechu^b

¹School of Mechanical and Industrial Engineering, Addis Ababa Institute of Technology, Addis Ababa University, Addis Ababa, Ethiopia

²School of Mechanical and Industrial Engineering, Addis Ababa Institute of Technology, Addis Ababa University, Addis Ababa, Ethiopia

*Corresponding Author's Email: getnetbelie@gmail.com, tilahunigussie2008@gmail.com

ABSTRACT

That there is an imbalance of electricity demand and supply in Ethiopia is known. Development of the Micro hydro power (MHP) system is an important technology to solve the problem. The main objective of this study was to do modelling and simulation of a micro-hydropower system for rural electrification in the case of Temecha River, Ethiopia. Yearly flow data were collected from Ethiopian Basins Development Authority and used to estimate the design flow rate. Next, modelling and simulation were done by using MATLAB SIMULINK. Some of the SIMULINK results were power and flow duration curves, and others. The nethead and design flow rates were found to be 16.34m and 0.5731m³/s, respectively. Based on the preliminary analysis, the turbine selected for the site is a Kaplan turbine. It is found that, the power output of this system is greater than the electricity demand of the selected site for 346 days of the year. Thus, the system is found to be efficient in terms of generated electrical power as compared to similar works reported in the literature. The scale of the design can be re modified to be implemented in other remote areas having river resources.

Keywords: - Electrical Power, Flow Rate, Kaplan Turbine, MATLAB SIMULINK, MHP, Simulation]

INTRODUCTION

According to a report by the World Bank[1], Ethiopia is the second most populated country in Africa with an estimated population of 114,963,583, next to Nigeria. The country has one of the fastest-growing economies in the world. Even though the demand for electricity is dramatically increased, the generation of power has not yet increased at the same proportion.

MoWIE also noted that[2] about 56% of the total population lack electricity access. The lack of electricity in these areas affects the daily routines of the inhabitants who seek to earn a living [3].

The MHP is a class of hydropower plant system that generates power within a range of 11 to 500 kW. A MHP is categorized under run-of-river, small head, single purpose, and base load plant. One of the main reasons for MHP system development is due to the high demand of electricity in rural areas where small streams of water are locally available in many areas of Ethiopia. These systems have been used for a long time, particularly in the rural villages of developing nations. It can provide the best solutions to the sustainable development goals by providing electricity to support the local economy, education, health, and food and communications systems. To ensure their cost competitiveness for deploying a large number of systems in the future, they

require further technological advancements, primarily the cost reductions and improvements in efficiency of MHP systems. Within this broader context of sustainable development, the aim of this research was to do modelling and simulation of a MHP system for rural electrification using MATLAB SIMULINK software. Technology wise, the system has additional features which will make it more valuable in the current market and provides an advantage for people living in rural areas[4].

Kilimo, A. S. G., and Kahn, M. [5] have highlighted the possibility of using low-cost small hydropower plant that can supply power to communities which have small hydro potentials. Finally, the authors proposed the use of the merits of both synchronous and induction generators to reduce the investment and maintenance cost of the plant. If these are implemented properly, the plant is expected to be of low cost and hence, an economically viable power source for rural electrification.

According to some studies [6, 7], the steps followed in MHP developments include site visits, data collection, measurements, field surveys, meetings with local populations, and analyses.

A study on “Analysis of Micro Hydropower Generation for Rural Electrification”, showed that the fixed blade axial flow propeller turbine was one of the most cost-effective turbine options for the low head scheme [8]. As the paper states that in Loi Unn micro-hydropower project, 7 turbine-generator sets were installed. The capacity of the set was 3kVA (2.4 kW). Then, the total installed capacity was 21 kVA (16.8 kW). And, the utilized power was 13.8kW. Generally, the daily operating time was from 6 pm to 6 am because Loi Unn stream was enough to generate micro-hydropower throughout the whole year. But, in the rainy season, the excess water was diverted to the other side of the Loi Unn stream.

After the implementation of the research on MATLAB Simulink software, the results that

are found in the literature [8, 9] are that the turbine power and speed were directly proportional to the gross head, but there were specific points for maximum power and maximum speed in case of water flow variations.

In [10], the author describes some problems related to energy crisis such as oil crisis, climatic change, electrical demand, and restrictions of wholesale markets a risen worldwide that leads to the increment of difficulties. This study aimed to suggest the need for technology alternatives that are used for generating electricity as near as possible of the consumption of site, using renewable and environmentally friendly energy sources such as wind, solar, and hydro-electric power plants. The system that has been done on this study is supplying power common electrical three-phase parallel RLC load. Finally, models were simulated using MATLAB Simulink. The simulation results show that with the proper choice of governing system for micro-hydro power plant leads to proper load sharing, constant voltage output, and constant speed with a variety of load values.

Additionally, in [11] the authors worked on “simulation and implementation of micro-hydro generation for small rural loads.” This study aims to develop a MATLAB/Simulink block of a simple run-off river micro-hydro system that could be used to simulate electricity generation at any location where the water resource and site conditions are suitable. They used data like water head, water flow and energy demand needed as input to the developed simulation models. Finally, the simulation results of the variation of the rotor angular velocity, the electromagnetic torque, and the stator voltages were included in their study.

Even though several works can be found for the micro-hydropower system in the literature, there is still a gap that is unsolved, the access of electricity distribution to rural areas like in Amhara region, Ethiopia.

MATERIALS AND METHODS

MATLAB SIMULINK was used for the simulation analysis of the system. Besides, the task slike site selection, data collection, data analysis and others were done to finalize the modelling and simulation of a MHS for rural electrification in the case of Temecha River, Ethiopia.

The site is located at 10.5150N and 37.4870E. 345km far from Addis Ababa, Ethiopia to the North West and 285km far from Bahirdar, capital city of Amhara Regional state to the South East. The site elevation is within the range of 950 to 2800 mean sea levels [4]. The

site selection was based on the scarcity of electricity access in the area and the all year-round flow of the River.

The first step of this research after selecting potential site was collecting technical data (Head and flow rate) that were used for MHP development. Following this, the design approach combining theoretical expressions, extensive simulation and modeling were done. Finally based on the site data, method of turbine selection, determination of flow duration curve (FDC) and modeling each component of MHP has to be made and discussed. The methodologies that were followed to accomplish this research are summarized in Figure 1.

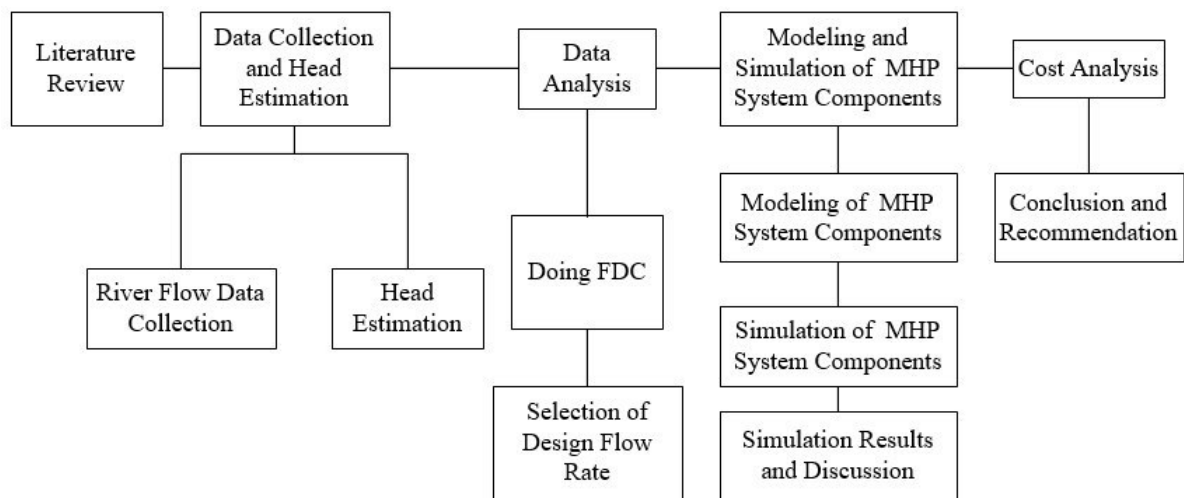


Figure 1 Methodology Flow Chart

RESULTS AND DISCUSSIONS

Load Demand Analysis

Table 1 shows the electricity demand analysis for the selected rural area. As seen from Table 1 and Figure 2, the peak load was around 72.72kW, the average load was 20.02 kW, and Table 1 Summary of Load Demand Analysis

the minimum load was 0.72kW. In this case, the design analysis was done by taking the peak load value.

Time Interval	Load in kW	Time Interval	Load in kW
7:00AM-8:00AM	0	7:00PM-8:00PM	72
8:00AM-9:00AM	0	8:00PM-9:00PM	72
9:00AM-10:00AM	0	9:00PM-10:00PM	0
10:00AM-11:00AM	0	10:00PM-11:00PM	0
11:00AM-12:00PM	0	11:00PM-12:00AM	0
12:00PM-1:00PM	72.72(Peak Load)	12:00AM-1:00AM	0
1:00PM-2:00PM	0.72	1:00AM-2:00AM	0
2:00PM-3:00PM	36.72	2:00AM-3:00AM	0
3:00PM-4:00PM	36	3:00AM-4:00AM	0
4:00PM-5:00PM	36	4:00AM-5:00AM	0
5:00PM-6:00PM	36.72	5:00AM-6:00AM	23.16
6:00PM-7:00PM	72	6:00AM-7:00AM	22.44

Figure 2 indicates the summary of the load analysis for the selected rural areas. It was found out that, the area has around 1200 houses without access to electricity. The purpose of the

electricity is for lighting, mobile charging, TV, microphones, and to drive machines like mill machine.

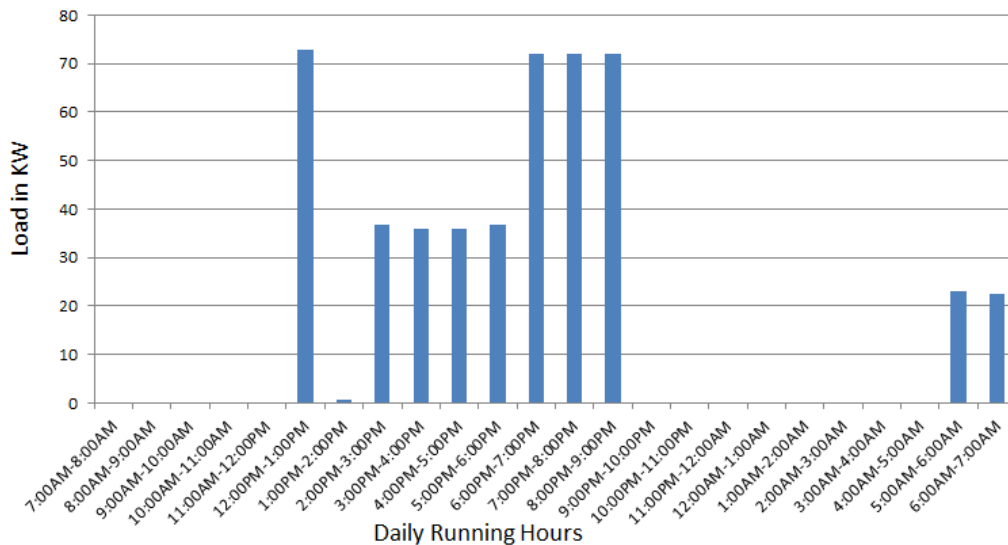


Figure 2 Load Duration Curve of the Site

Determination of Flow Duration Curve

The flow duration curve (FDC), was used to assess the expected availability of flow over the time and the power and energy at a site and to

decide on the “design flow” in order to select the turbine. Therefore, a stand-alone system such as a small hydropower system should be designed according to the flow that is available all year round; this is usually the flow during the dry and wet season. It is possible that some

Modeling and Simulation of a Micro-hydropower System for Rural

streams could dry up completely at that time [12].

Ideally, minimum flow over the year should be taken to calculate the design flow to ensure that power is available year-round. Thus, only a fraction of the available flow in the stream is used for power generation [12].

Firm flow is the flow being available $p\%$ of the time, where p is a percentage specified by the user and usually between 90% and 100% [12].

Minimum flows were determined according to the methodology applied elsewhere [12, 13]. For this research, the % of time considered for firm and design flow were $Q_{100\%}$ and $Q_{95\%}$, respectively. The FDC, Figure 3, depicts, the flow rate versus % of time of the selected river data, the flow that could be available 95% of the time or more [13]. Thus, the resulting flow value for firm flow rate was $0.49\text{m}^3/\text{s}$ and that of the design flow rate was $0.5731\text{m}^3/\text{s}$.

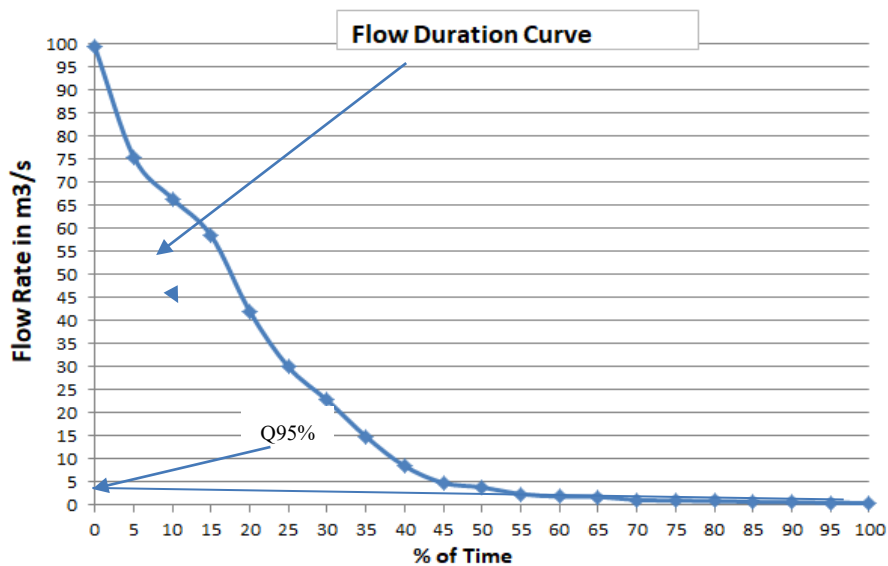


Figure 3 Flow Duration Curve of *Temecha* River

Figure 4 was developed with MATLAB SIMULINK software. It contains the 12-month flow rate of the site which are less than or equal to the design flow rate. As indicated in the figure, greater changes were noted for the flow rate of 11 months of the year which was equivalent to that of the design flow rate. These are represented by the horizontal line. And also, the flow rate of February was less than

that of the design flow rate for 16 days of the month. Similarly, the flow rate of March was less than the design flow rate for 3 days of the month. The flow rate of April was less than that of the design flow rate for 1 day. For the flow rates that were equal to the design flow rate, the system gets enough flow rate for those days without interruption.

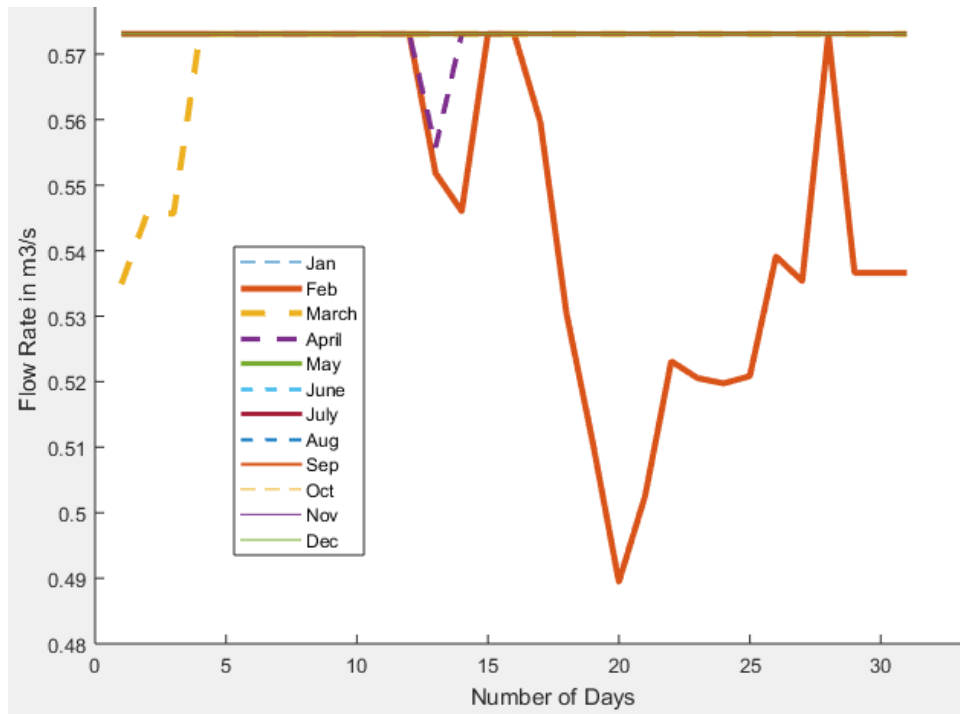


Figure 4 Flow duration curve in the penstock

Determination of Flow Head

The selected site, *Temecha* River has no head by nature, but it has available flow rate throughout the year. Therefore, based on the literature [16], a small weir was constructed for the site based on the following analysis.

Calculation of the Turbine Efficiency at each Flow:-

- The specific speed adjustment to peak efficiency (\hat{e}_{nq}) is

$$\hat{e}_{nq} = \left(\frac{n_q - 170}{700}\right)^2 \tag{1}$$
- Runner size adjustment to peak efficiency (\hat{e}_d) is

$$\hat{e}_d = (0.095 + \hat{e}_{nq}) (1 - 0.789 * d^{-0.2}) \tag{2}$$

- Turbine peak efficiency (e_p) is

$$e_p = 0.905 - e_{nq} + e_d - 0.0305 + 0.005R_m \tag{3}$$

where, R_m ,

$$R_m = \frac{\text{Turbinemanufacturer designcoefficient}}{(2.8 \text{ to } 6.1, 4.5 \text{ is used by default})}$$

- Peak efficiency flow (Q_p)

$$Q_p = 0.75Q_d \tag{4}$$
- Efficiency at flows above and below peak efficiency flow (e_q)

$$e_q = \left[1 - 3.5 \left(\frac{Q_p - Q}{Q_p}\right)^6\right] e_p \tag{5}$$

- The available mechanical power produced by the turbine is given by

$$P_{avail} = \rho g Q (h_g - (h_{hydr} + h_{tail})) e_{t,Qd} \tag{6}$$

Modeling and Simulation of a Micro-hydropower System for Rural

The actual power from the turbine (P_{design}) as a function of design flow rate is given by:

$$P_{d,turbine} = \rho g Q_d h_g (1 - (h_{hydr} + h_{tail})) e_{t,Qd} \quad (7)$$

- Available power the MHP plant
The power available and the flow rate are related with the equation below

$$P_{avail} = \rho g Q (h_g - (h_{hydr} + h_{tail})) e_{t,Qd} e_g (1 - l_{trans}) * (1 - l_{para}) \quad (8)$$

The actual power from this micro hydropower system of (P_{design}) as a function of design flow rate by assuming generator efficiency of 95% is

expressed as:

$$P_d = \rho g Q_d h_g (1 - (h_{hydr} + h_{tail})) e_{t,Qd} e_g (1 - l_{trans}) * (1 - l_{para}) \quad (9)$$

Where, $e_{t@Qd}$ =

turbine efficiency at the design flow rate = 86.23%

e_g = generator efficiency = 95%,

Hydraulic losses h_{hydr} = 7%,

Transformer losses l_{trans} = 2%,

Parasitic electricity losses l_{para}

= 3%, and tail race losses h_{tail} = 7% are assumed for this case.

Table 2 shows the summary of the turbine parameters as the gross head varies. The

analysis was done to estimate the gross head for the selected river to satisfy the peak load required by the area.

Table 1 Turbine parameter analysis at variable gross head

Gross head, H_g (m)	Net head, H_n (m)	Turbine runner size, d (m)	Specific speed, n_q	Turbine Speed, n (r.p.m)	Specific speed adjustment to peak efficiency (\hat{e}_{nq})	Runner size adjustment to peak efficiency (\hat{e}_{ad})	Turbine peak efficiency (e_p)	Peak efficiency flow (Q_p) (m^3/s)	Available power at the design flow rate, P_d (Kw)	MHP System Available Power in KW
10	8.6	0.354	273	616	0.0216	0.0033	0.879	0.403	42.5	38.4
12	10.32	0.354	249	642	0.0127	0.0031	0.887	0.403	51.5	46.5
14	12.04	0.354	231	665	0.0075	0.0029	0.892	0.403	60.4	54.6
16	13.76	0.354	216	687	0.0043	0.0028	0.896	0.403	69.3	62.6
18	15.48	0.354	203	706	0.0023	0.0028	0.898	0.403	78.1	70.5
19	16.34	0.354	198	716	0.0016	0.0028	0.898	0.403	82.5	74.5
20	17.2	0.354	193	725	0.0011	0.0027	0.899	0.403	86.9	78.5

As expressed in the demand analysis, the peak load was 72.72kW. As seen in Table 2, the turbine design parameters that satisfies this

peak load requirement has 19m gross head and 0.5731m³/s of design flow rate. Therefore, based on the above analysis for this case, a net head value of 16.34m was considered.

Selection of Standard Components

Selection of Turbine

The parameters values used for the selection of turbines are design flow rate, $Q_d=0.5731\text{m}^3/\text{s}$ and net head up to 16.34m. Therefore, from turbine selection chart shown in Figure 5, the

type of turbines may be Cross flow, Kaplan, and Propeller. For this case, Kaplan turbine was selected, an axial flow reaction turbine suitable for low heads. It was selected as it can handle the variation of flow efficiently and since it is more efficient than propeller and bulb turbines.

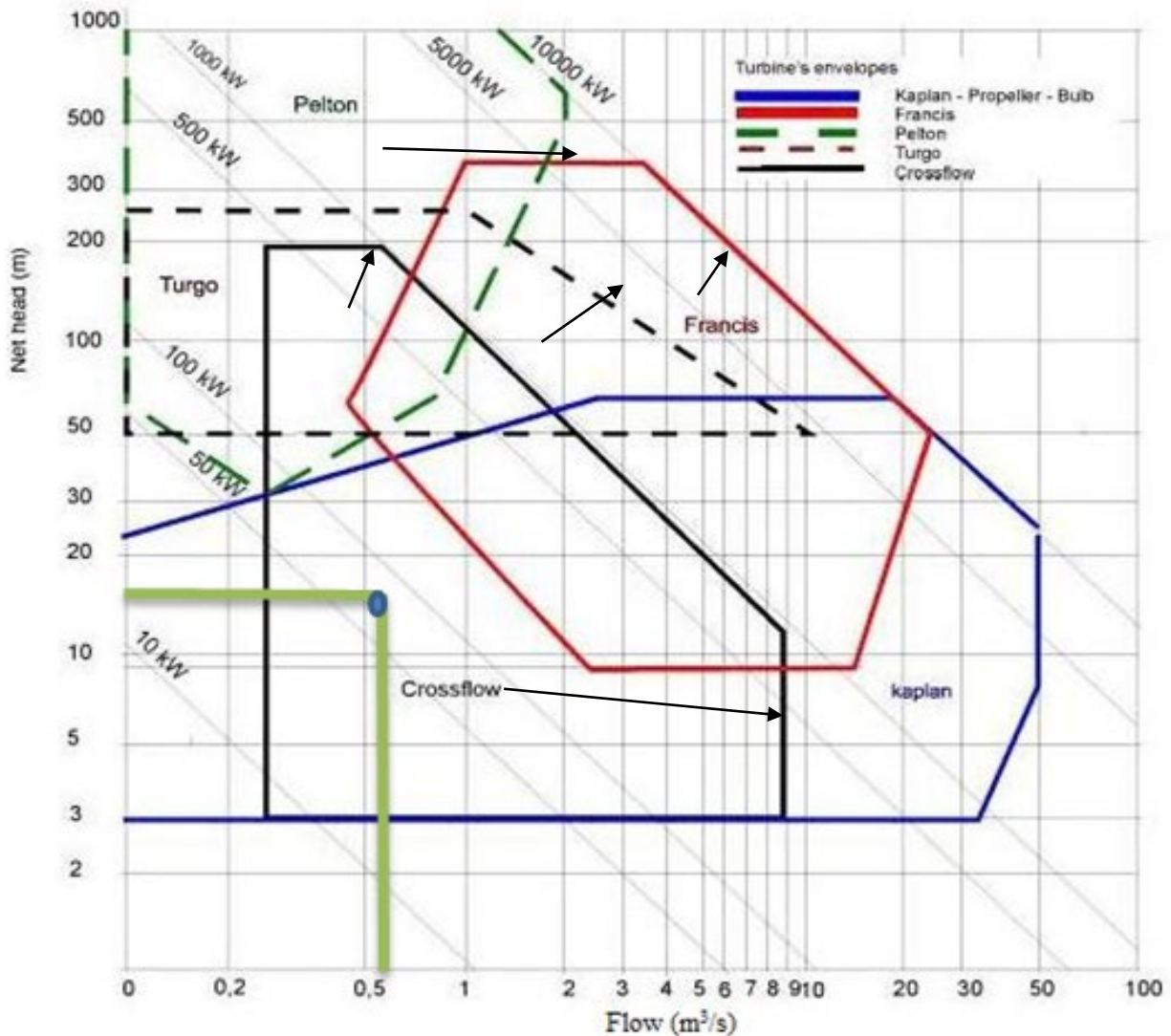


Figure 5 Turbine selection chart based on net head and flow rate [14]

Selection of Generator

Generator in hydropower system is used to convert the mechanical energy produced by the

hydraulic turbine into electricity. Two types of generators are used for hydropower systems [13]. These are synchronous and asynchronous generators. Synchronous generators are used

Modeling and Simulation of a Micro-hydropower System for Rural

for large hydropower system capacities more than 10MW, whereas Induction generators are used for low power capacities less than 10MW. In [15] the authors states that, in Hydropower system either the induction or synchronous generators are used. In small hydro power systems like MHP plant, induction generators are recommended and the size of the generator

is determined by the output power of the turbine [15]. Since, this research has aMHP system with capacity power less than 10MW, which is 74.5KW, induction generator type that has a capacity of 75kw is selected for this system.

RESULTS AND DISCUSSIONS

Mechanical Power Curve

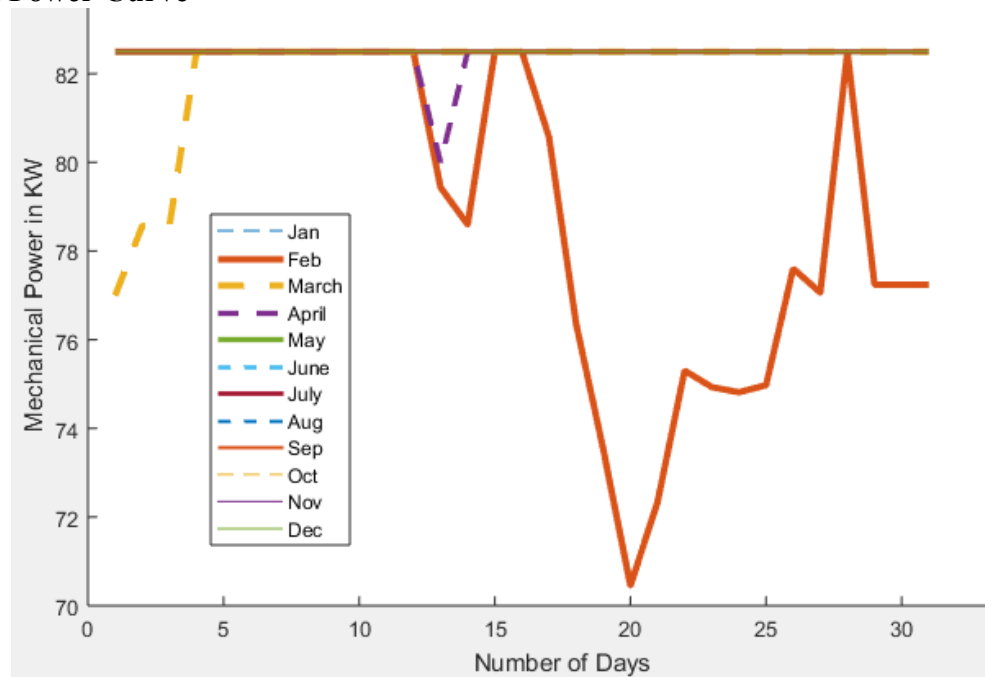


Figure 6 Turbine mechanical power output curve (mechanical power vs. number of days)

As shown in Figure 6, the mechanical power output from the Kaplan turbine was around 82.5kW, which was represented by the horizontal line and below it for around 20days of the year. For example, the mechanical power produced during the month of February was less than the maximum one for 16days. This was because the flow rate of this month was less than that of the design flow rate. On the

other hand, for March, the mechanical power produced was around 82.5kw for 27 days and less than that for the remaining 3 days. For April, the turbine output was 82.5 kW for 29 days and less than that for 1 day of the month. Generally, the above variation of the turbine output power was caused due to the flow rate variation around the year.

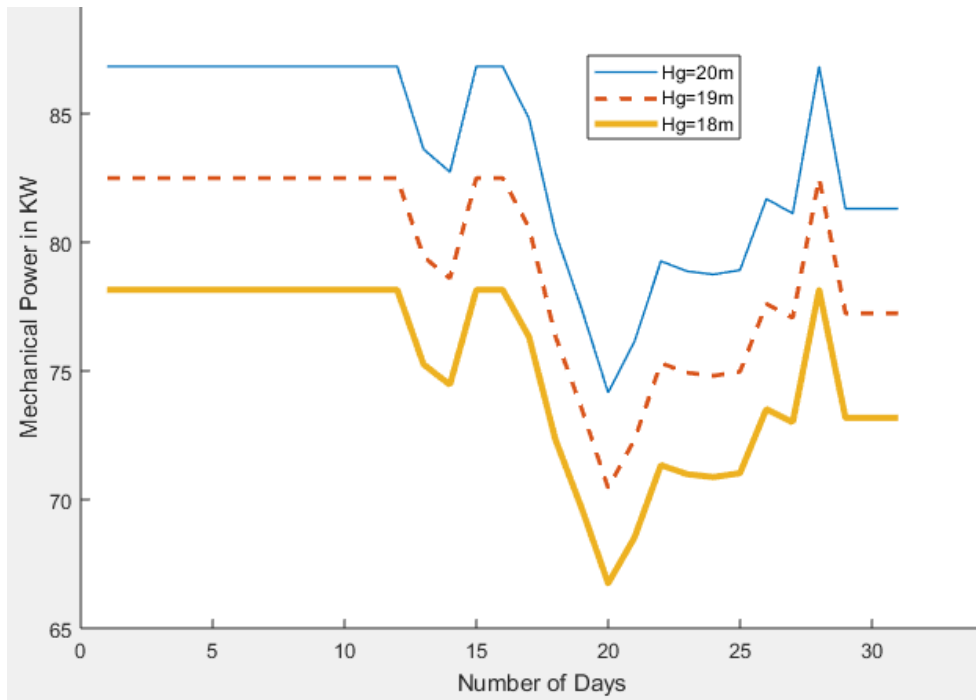


Figure 7 Mechanical power vs number of days for February month at different values of Gross Head

Figure 7 shows the variation of mechanical power with the number of days at different values of the gross head. Obviously, one can

see that the mechanical power increases as the flow head increases.

MHP System Power Curve

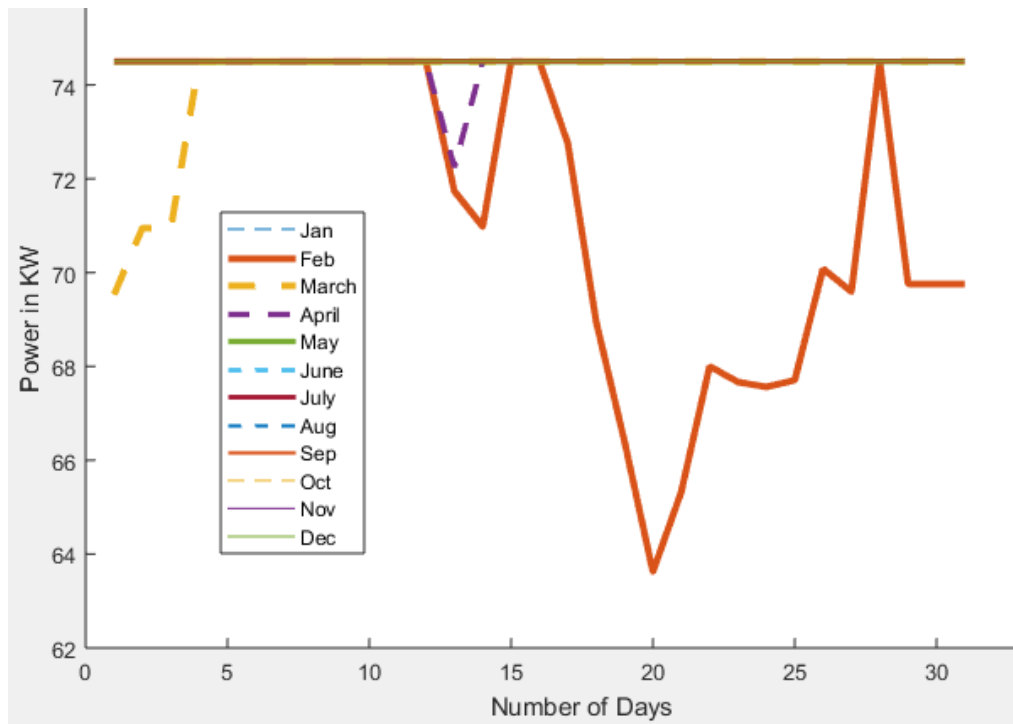


Figure 8 MHP system output power curve

Figure 8 show that the MHP system output power versus the number of days of the year for each month.

As seen in the figure, the maximum power output of the system was found to be 74.5 kW. This numerical value was constant for 11 months of the year.

For the months of February, March and April, the output power was below the maximum

for 16, 3 and 1 days, respectively as the river flow rate was less than the design value in these days. Generally, the system satisfies the demand amount for 346 days of the year.

Thus, if the monthly energy requirements are greater than that could be generated by this system, then the consumption need to be reduced so that it at least matches the available energy but in some cases, electronic load controller connected to the generator can be used to give the balance.

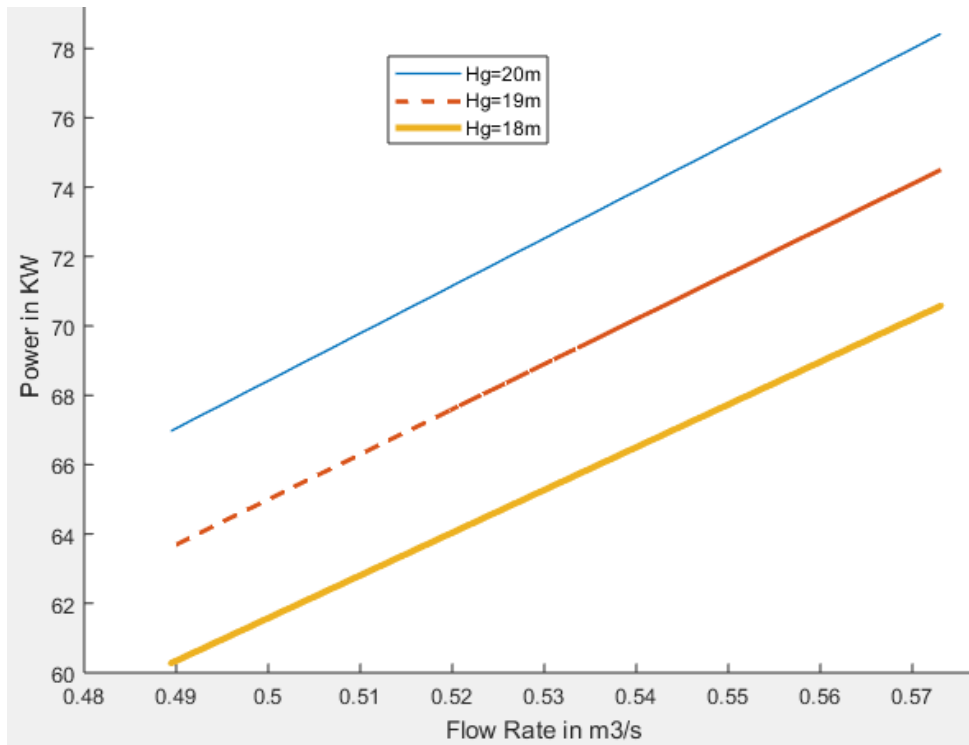


Figure 9 Final system output power versus flow rate of February at different values of Gross Head

Figure 9 shows the MHP System power output versus flow rate at different flow head values of the site.

The result shows that as the flow rate increases, the power output also does. And also, as the flow head value increases, the power output also does. Therefore, the system power, flow rate, and flow head have a direct relationship with each other.

CONCLUSIONS

MHP system solves rural electrification problems in remote areas. Therefore, the main objective of this research was to model and simulate the MHP system in the case of the *Temecha* River.

The uniqueness of this research from previous works was summarized below.

As seen in the simulation result, Figure-8 shows that with a 16.34m net head and 0.5731m³/s design flow rate, the electricity produced is up to 74.5 kW of power, which is enough to be more than current demand of 72.72 kW of electricity for the site.

From these results, one can conclude that by implementing this MHP system, 74.5 kW electricity can be produced for around 346 days of the year. In general, by implementing such an MHP system, around 1200 families can get electricity access for lighting, mill machine and mobile phones.

As the population and their economic activities increased, the researcher recommends the society to implement such additional Micro Hydropower systems with in a small distance of the original one.

Modeling and Simulation of a Micro-hydropower System for Rural

Most importantly, a general awareness and technical understanding of successful Micro-hydro power technology can be developed and fostered at the local and regional levels so that rural electrification projects can be implemented effectively. Finally, this study recommends capacity building in Micro hydro power technology, transformation of research findings into real products to solve rural electrification problems.

CONFLICT OF INTEREST

The authors declare that they have no conflicts of interest.

ACKNOWLEDGMENTS

The authors would like to address the acknowledgment of the Ethiopian Basins Development Authority Company, Addis Ababa, Ethiopia, for supplying the river flow data of both *Temecha* and *Gudla* River.

REFERENCES

- [1] World Bank, <https://data.worldbank.org/indicator/SP.POP.TOTL?locations=ET>, 2020.
- [2] Ethiopian Ministry of Water, Irrigation and Electricity, "National electrification program 2.0. Integrated planning for universal access", Technical report, 2019.
- [3] Kusakana, K., Munda, J. L., and Jimoh, A. A. "A survey of technologies increasing the viability of micro-hydropower as a cost-effective energy source for remote communities in South Africa", IEEE AFRICON Conference, September 5–9, 2009.
- [4] Walegn Dilnesa, "Assessing the Impacts of Land use / cover Change on the Hydrological Response of Temcha watershed , upper Blue Nile basin , Ethiopia", International Journal of Scientific Research in Civil Engineering, vol. 2, no.5, 2018, pp. 10-20.
- [5] Kilimo, A.S.G., and Kahn, M.T.E., "Small Hydro for Rural Electrification", 2012. this is incomplete
- [6] Anaza, S.O., Abdulazeez, M.S., Yisah, Y.A., Yusuf, Y.O., Salawu, B.U. and Momoh, S.U., "Micro Hydro-Electric Energy Generation- An Overview", American Journal of Engineering Research. (AJER), vol. 6no. 2, 2017, pp. 5–12.
- [7] Signe, K.E.B., Hamandjoda, O. and Nganhou, J. "Methodology of Feasibility Studies of Micro-Hydro power plants in Cameroon: Case of the Micro-hydro of KEMKEN", Energy Procedia, vol. 119, 2017, pp. 17-28.
- [8] Ram, S. and Ya, A.Z., "Analysis of Micro Hydropower Generation For Rural Electrification" incomplete the confenece is not known
- [9] Nasir, B.A., "Design of Micro - Hydro-Electric Power Station", International Journal of Engineering and Advanced Technology (IJEAT), vol. 2, no. 5, 2013, pp. 39-47.
- [10] Auwal Abubakar Usman, R. A. A. Modelling and Simulation of Micro Hydro Power Plant Using MATLAB Simulink. January, 260–272, 2018.
- [11] Kusakana, Kanzumba, Vermaak, H.,

Getinet Endale and Tilahun Nigussie

&Yuma,G.P.

Simulation and Implementation of Micro Hydro Generation for Small Rural Loads. April. 2018.

- [12] Arthur, J. K. Assessment of a typical small hydropower site for rural electrification in the western region of Gana. *Master of Science in Renewable Energy Technologies, KNUST,2014.*
- [13] Davis,S.,&Graham,S.*Micro-Hydropower System's A Buyer's Guide,2004.*
- [14] Sangal, S., Garg, A., & Kumar, D. Review of Optimal Selection of Turbines for Hydroelectric Projects. *Review of Optimal Selection of Turbines for Hydroelectric Projects, 3(3), 424–430,2013.*
- [15] Srpčić, G.*Selection of induction generator for a small hydropower plant “ Sušica”,XIV International PhD Workshop. October, 20–23,2012.*
- [16] Energybc.ca, “*Run of River Power - Energy BC.*”,2018.

PREDICTIVE MAINTENANCE OF BALL BEARINGS USING CONVOLUTIONAL NEURAL NETWORKS (CNN)

Arsema Derbie and Kibru Temesgen

School of Mechanical and Industrial Engineering, Addis Ababa Institute of Technology, Addis Ababa University, Addis Ababa, Ethiopia

Corresponding author:

ABSTRACT

To this day, numerous maintenance actions follow preventive and run-to-failure methods. In this work, it has been attempted to show the power of predictive maintenance (PdM) from vibration data using a machine learning technique implementing convolutional neural networks (CNN). Actual data was collected from six different bearings on a machine element fault analysis test rig. The bearings were of the ball bearing type, where one of them was healthy and the rest were faulty at the inner race, the outer race, the rolling element, or a combination of these three, and another had severe damage at either the rolling element or the rings. From the vibration signatures specific to the health status of the bearings, a powerful deep learning convolutional neural network model was built. The model was able to successfully classify the states of bearings with accuracy values ranging between 76.7 and 99.9% based on unseen data. The results indicate that this CNN model can be used as a diagnostic tool for undertaking maintenance operations.

Keywords: *CNN, predictive maintenance*

1 INTRODUCTION

Monitoring the state of machinery and its health condition is one of the top priorities of companies since a huge amount of money is invested in equipment. Companies want their equipment to last as long as possible,

and predictive maintenance is the best and most prospective way of ensuring that. With the advancement of artificial intelligence (AI), the lowering cost of sensors, and the increasing connectivity among devices because of the explosion of the internet, now is the time to take advantage of AI for maintenance.

A maintenance program often falls into a few categories, each with its own set of challenges and benefits. PdM is one of them. It is a collection of approaches that employ condition-monitoring technologies to monitor a machine's performance and discover potential flaws before it breaks. Too early maintenance can result in money being spent unnecessarily, while too late maintenance might result in catastrophic equipment damage.

Recently, studies on bearing prognostics can be seen as a problem of pattern recognition, and several research attempts have been made to develop techniques for machine health monitoring [1]. Hrnjica et al. [2] describe an example of an explainable AI (XAI) in the form of a PdM scenario for manufacturing. PdM is performed using machine learning algorithms to predict when maintenance should be performed on equipment before it fails. The authors used CNN to predict when a bearing will fail based on vibration data. Due to improvements in machine learning algorithms and the accessibility of vast volumes of data, the application of AI in

PdM has grown in popularity in recent years.

Unexpected bearing failures may force companies to pay for repairing and replacing the bearing and adjacent components, which may also sustain damage, such as housings and shafts. Bearing failures reduce a plant's operating efficiency, increase downtime, drive the cost of operations up, and, in the worst cases, may injure workers. Unplanned maintenance increases the chance of worker injury. With workers, 28% more likely to have an accident at work when performing reactive maintenance over proactive maintenance, the impact that premature bearing failure can have on worker safety is clear [3].

In manufacturing plants, optimal maintenance strategies are necessary to ensure system reliability, reduce cost, avoid downtime, and maximize the useful life of a component [4]. According to a recent article, unplanned downtime caused by poor maintenance strategies reduces a plant's overall productive capacity by up to 20 percent and costs around \$50 billion each year [5].

Many researchers have studied condition monitoring (CM) using CNN and Deep Neural Networks (DNN). Zhang et al. [6] showed the domain adaptability of classifying different bearing vibration signals using CNN. It is one of the most notable deep learning models due to its shared weights and ability for local field representation [7]. CNN can extract the local features of the input data and combine them layer by layer to generate high-level features. In the field of predictive maintenance, CNN has shown dramatic capability in extracting useful and robust features from monitoring data. For one-dimension (1D) monitoring signals, Qin et al. [8] built an end-to-end 1D-CNN that

reflected the raw vibration signals to fault types. The result showed that the proposed model was able to achieve about 99% accuracy through hyperparameter tuning. Furthermore, the applications of CNN in remaining useful life prediction have been widely investigated.

There has been immense success in the application of CNN to image and acoustic data analysis. In this paper, rather than preprocessing vibration signals to de-noise or extract features, they investigated the usage of CNNs on raw signals; in particular, they tested the accuracy of CNNs as classifiers on bearing fault data by varying the configurations of the CNN from a one-layer up to a deep three-layer model. They also inspected the convolution filters learned by the CNN and showed that the filters detect unique features of every classification category. In addition, they studied the effectiveness of the various CNN models when the input signals were corrupted by noise [9]. Guo et al. [10] proposed a deep hierarchical architecture of CNN in which original data was converted into 2D data to classify bearing faults and their sizes. Many of the published works of CM with CNN approaches show very high accuracy, but they were mostly tested on the same dataset.

Access to datasets is a difficulty while investigating machine learning (ML) and deep learning (DL) algorithms for fault diagnosis because it is difficult and expensive to build a realistic mechanical fault dataset-producing test-bench. The dataset created by Case Western Reserve University (CWRU) is the most well-known and easily accessible dataset for vibration-based rolling bearing failure diagnostics and has been used as the standard reference in numerous papers. In their research, Neupane and Seok [11] examined numerous articles on deep learning algorithms employing the CWRU dataset. Smith and Randall [12]

studied the complete CWRU dataset and provided benchmark recommendations for diagnostic methodology.

Mohammad et al. [13] proposed a time-moving segmentation window to segment the raw vibration signal, and the segmented signals were decomposed up to two levels using the discrete wavelet transform (DWT). After that, decomposed signals were converted into grayscale images to train and test the proposed CNN model. To verify the performance of the model, the CWRU bearing dataset and the MFPT dataset were used. The proposed CNN model achieved the highest accuracy in terms of performance under different load conditions as well as in noisy situations with varying signal-to-noise ratio values. The experimental findings showed that the proposed system was effective and extremely dependable in detecting bearing faults. Junjie et al. [14] used a CNN based on improved soft maximum loss (ISM-CNN). The constructed CNN could learn more subtle features from the bearing signals, thereby improving the accuracy of bearing signal classification. Besides, the algorithm proposed in the same paper expanded the training data set to a certain extent, so that the parameters of the ISM-CNN could be better fitted. They validated the effectiveness of the proposed algorithm on the CWRU open dataset and performed ablation experiments to prove it.

The target of this research study was to develop a PdM model for ball bearings using CNN to predict the health status of bearings before the equipment fails by using the vibration signal generated from the bearings.

2 MATERIALS AND METHODS

2.1 Test-rig and Dataset



Figure 1 Experimental test-rig of PT 500.12

Figure 1 shows the experimental setup that was used. The shaft was connected to a motor through a coupling. The motor could be operated to a maximum speed of 4100 rpm. The shaft was connected to the two bearing blocks. The bearing block immediately adjacent to the motor housed a normal (healthy) bearing, which was not changed during the entire data acquisition process. The second bearing block housed bearings with different types of damage during the measurement. Bearings were fixed into the block by using a retaining ring. The bearing blocks had spaces for the mounting of accelerometers.

An accelerometer was fixed to the bearing block in such a way that there would be no relative motion between them. The threaded section was located on the top and sides of the bearing block to measure both the horizontal and vertical vibration. The accelerometer (B&K Vibro's AS-020) was used to measure the vibration characteristics. It was mounted on the bearing block that contained the damaged bearings.

The accessory setup contained six roller bearings, on which different faults could be detected and explained. The accessory setup was mounted on the base plate of the machinery diagnostic base system PT

500.12 roller bearing faults kit. A photo-contact tachometer was used to measure the speed of the shaft. Six different bearings with different fault types were used in this test. After mounting them on the bearing block, vibration patterns were recorded for each type.

The test was done at a shaft speed of 1500 rpm and a torque of 0.1 Nm. The vibration data was recorded at a sampling rate of 15 kHz for 10 seconds, which resulted in 150,000 data points. The output of the accelerometer was in units of voltage. This voltage was then converted into a vibration unit known as "G," which is an acceleration unit. The conversion was done by using the sensitivity of the accelerometer. The sensitivity of an accelerometer is defined as the ratio of the output voltage to the acceleration being measured. After the conversion, the dataset was directly fed into a CNN architecture without the need for any preprocessing.



Figure 2 Six types of Bearings (SKF 6004) with different health status

The faults were created by introducing defects in the bearings. The defects were introduced using an electro-discharge machining (EDM) by GUNT, the manufacturer of the PT 500.12 test-rig process to create artificial defects in five different parts of the bearings.

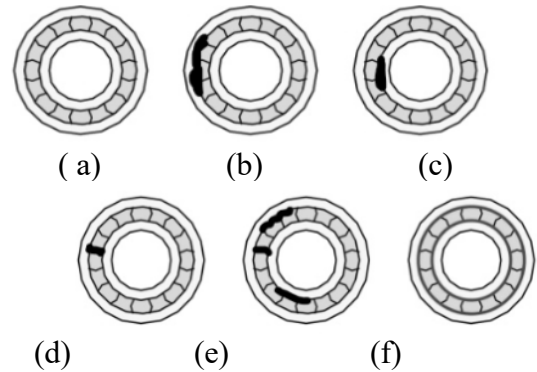


Figure 3 Types of faults and their locations; a) healthy bearing, b) damage on outer race, c) damage on inner race, d) damage on roller body, e) damage on roller body, outer and inner race, f) heavily worn bearing

2.2 Proposed CNN Architecture for Bearing Fault Classification

CNN uses the convolution operation in its architecture. This operation was used to extract features from the input data. The convolution of two functions f and g is denoted by $f * g$ and defined as the integral of the product of the two functions after one is reflected about the y -axis and shifted. The formula for the convolution operation is given by:

$$(f * g)(t) = \int f(z) f(t - z) dz \tag{1}$$

where f and g are two functions, t is a variable, and z is a dummy variable for integration.

ReLU is a non-linear activation function that is used in CNN. It is used to introduce non-linearity in the output of a neuron and helps prevent over fitting. This function can be represented as:

$$f(x) = \text{Max}(0, x) \tag{2}$$

A 1-D CNN with multiple (parallel) inputs of the same data was used for this study. Three different kernel sizes were used for the same input data. This was achieved by using three parallel convolutional layers. After the inputs passed through the three paths, they were combined and fed into a fully connected layer, which was followed by another fully connected layer and an output layer.

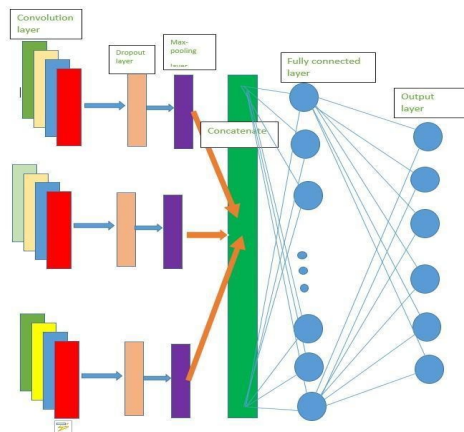


Figure 4 Proposed CNN architecture for 6 classes

2.2.1 Along upper path

A 1-D convolutional layer with 64 filters, with each filter having a kernel size of (200, 200), was used. A drop-out layer was used to avoid over-fitting, and the drop-out rate was set to 50%. This means that during each forward pass, 50% of the neurons were randomly deactivated. A max-pooling layer with a pooling size of 20 was also used. Max pooling would reduce the dimensionality of the output from the convolutional layers. This was important to make the model less sensitive to changes and more robust. It was equivalent to creating a lower resolution of the output while still retaining significant information. Networks with ReLU activation show better convergence, less vanishing, and fewer constant gradient

problems, which has made them the best choice on CNN.

2.2.2 Along middle path

1-D convolutional layer with 64 filters, with each filter having a kernel size of 100 by 100, was chosen. A drop-out layer of 50% and a ReLU activation function were used.

2.2.3 Along lower path

1-D convolutional layer with 64 filters, with each filter having a kernel size of (50, 50), was used. Similarly, a drop-out layer of 50% and a ReLU activation function were used.

Along each path, different kernel sizes and max-pooling sizes were used to help the model retain different information along each path, thus making it robust to changes in the data for which the model was expected to predict. The input, after passing along the three paths, was flattened and concatenated together. The concatenated output was fed into a fully connected layer with 100 neurons and the ReLU activation function. After passing through the fully connected layer, the input was fed into the output layer to produce the prediction.

2.3 Training the Model

The input data to the 1D-CNN was augmented using a window size of 4500 data points and a stride of 60 data points. So, one input to the architecture was a 4500-by-1 matrix representing 0.3 seconds of vibration duration. This was crucial in creating the large number of input data points that the model was trained on. The model was trained using the Google Compute Engine (GPU) through *Google Collaboratory*. The GPU provided by Google Colab is the Tesla K80 with 2496 CUDA cores and 12GB GDDR5 VRAM. This compute-optimized engine took no

more than 45 minutes to train the model, unlike typical CPU computers, which would have taken more than 6 hours to train. The model was trained for a total of 200 epochs. The model was normally trained until it no longer showed improvement in accuracy. For this particular work, the model converged at an epoch of around 200.

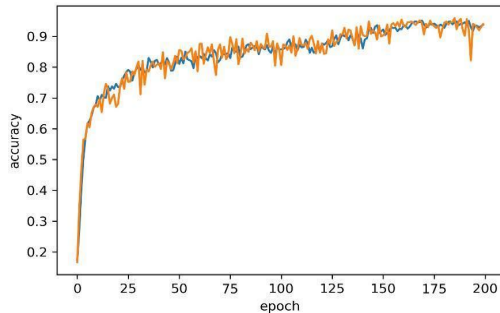


Figure 5 Training accuracy Vs number of epochs over time

3 RESULTS AND DISCUSSION

3.1 Prediction

Two rounds of data were taken for this test in different sessions. During each round of data acquisition, the bearings were disassembled from the bearing block and reassembled in place. The accelerometers were unmounted. The model was built using the first round of data. In this work, the test data on which the model was evaluated was entirely from a different session. The purpose of doing so was to test the robustness of the model on completely unseen data.

The results of the prediction are shown in the next sections.

3.1.1 Ball bearing fault

The vibration data from the second session was given to the model to make a prediction,

and the result was evaluated. The model was not trained on this data, but the class of the vibration data was known to be of the ball bearing fault type.

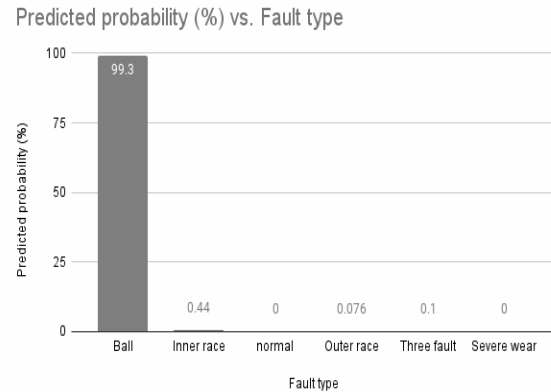


Figure 6 Ball fault Prediction on second round data

Accordingly, the model gave a probability of 99.3% that the bearing had a rolling element (ball) fault.

3.1.2 Inner race fault

A prediction confidence level of 92.7% that the bearing had an inner race fault was obtained.

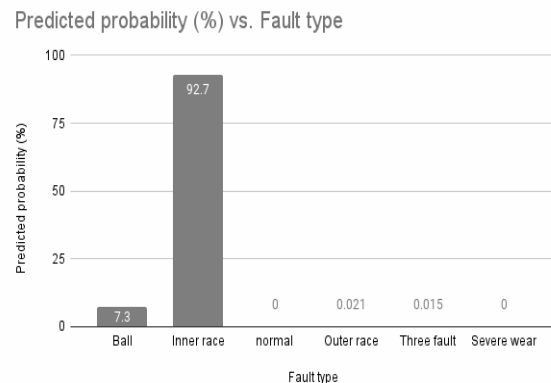


Figure 7 Inner race fault Prediction on second round data

3.1.3 Normal bearing

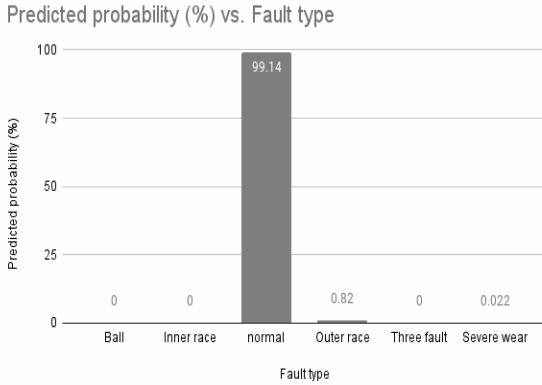


Figure 8 normal bearing Prediction on second round data

A probability of 99.14% that the bearing was normal was obtained.

3.1.4 Outer race fault

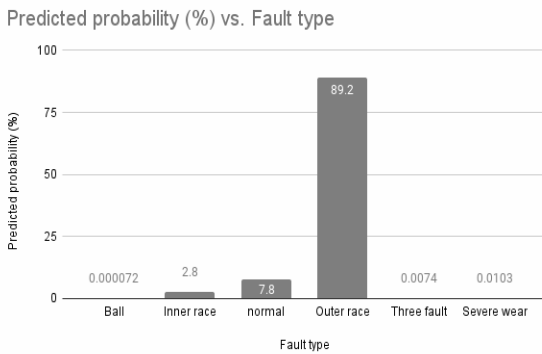


Figure 9 outer race prediction on second round data

The model gave a probability of 89.2% that the bearing had an outer race fault.

3.1.5 Combination of three faults

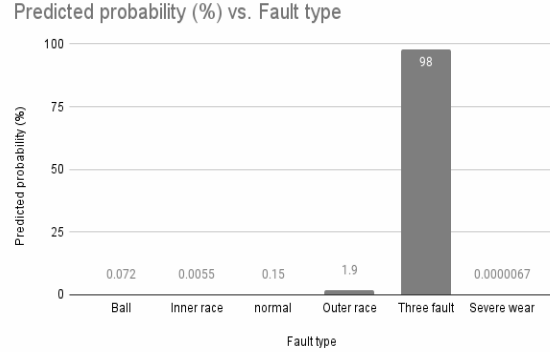


Figure 10 Combination of three fault prediction

The model gave a probability of 98% that the bearing had three fault combinations.

3.1.6 Severe wear faults

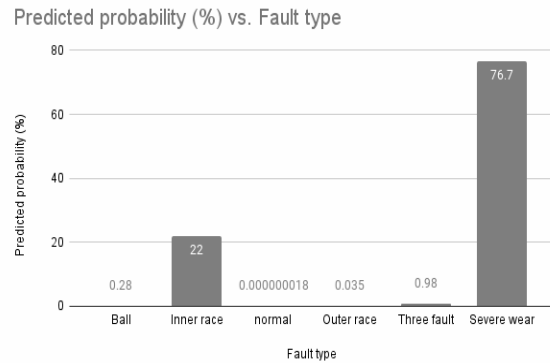


Figure 11 Severe wear fault prediction

The model gave a probability of 76.7% that the bearing had a severe wear fault.

3.2 Discussion

The prediction on the second round of data was quite satisfactory for all faults except in the case of severe wear. The model predicted the fault types with an accuracy of above 90% for most of the faults. The fault of the outer ring is usually difficult to predict because the rings are stationary and don't exhibit peculiar vibration patterns like

the rest of the components. However, on the outer race, an accuracy of 89% was obtained, which is a good result.

For companies, it is usually not that important to know what type of fault is going to occur. The most important question is the health status of the bearing (healthy or faulty). The accuracy of the normal bearing was above 99%. This is significant for increasing the reliability of the model. The model is not susceptible to giving false positive results. It would have been a bad result if the model had predicted a normal bearing status as faulty. This would mean that operations are not halted for maintenance.

Fairly good accuracy has been obtained without using tiresome preprocessing techniques that used to be performed on ML techniques. Especially for the normal bearing health status, the model predicts with an accuracy of 99.9%, indicating its dependability in identifying whether a bearing is healthy or faulty. The CNN was able to construct feature representations that assisted in the categorization of "normal" and "faulty" data, outperforming previous approaches, which relied on feature selection, and displaying a higher accuracy rate [1-5, 16, 19].

Many papers validate their work by setting aside 30% of their data, of which 70% is allocated for training their model's performance [11, 12, 15, 17-19]. This study, however, used an entirely different session dataset to validate the robustness of the model.

Two fault classes (outer race fault and severe wear fault) had the lowest prediction accuracy: 89.2% and 76.7%, respectively. As pointed out previously, the outer race doesn't rotate as much as the rest of the components; therefore, it doesn't exhibit the

peculiar vibration pattern associated with it. On the other hand, the severe wear fault doesn't have a localized fault, and the distribution of the fault over the whole surface doesn't make the bearing vibrate every cycle as with other fault types. Hence, this prevented the bearing from giving a purely distinct pattern.

The model's accuracy of over 99% in predicting the bearing's health status is a noteworthy accomplishment with broad ramifications for businesses that depend on machinery with bearings. Its excellent accuracy rate demonstrates the model's dependability in determining whether a bearing is in good condition or not. Outperforming earlier methods that depended on feature selection, the CNN was able to create feature representations that helped classify "normal" and "faulty" data. Also, this method does away with the necessity for time-consuming preprocessing methods that were previously utilized with ML techniques. The model's dependability in determining whether a bearing is healthy or faulty is demonstrated by its accuracy of 99.9% in predicting normal bearing health status.

The significance of this achievement cannot be overstated, as it has implications for increasing the reliability of machinery and reducing downtime due to unexpected failures. Companies can now have greater confidence in their machinery and plan maintenance schedules more effectively. This approach also eliminates the need for costly and time-consuming manual inspections that are often required to identify faulty bearings. The model's ability to predict normal bearing health status with an accuracy of 99.9% signifies its dependability in identifying whether a bearing is healthy or faulty and provides companies with greater confidence in their machinery.

4 CONCLUSIONS

The CNN framework proposed in this work can detect faults by using indicators that precede failures and advise maintenance. This work demonstrates the potential of deep learning methods for fault classification and bearing health condition monitoring.

This study has shown that although CNN networks were designed for image classification, they are sometimes even more powerful in classifying vibration patterns and tackling the problem of over fitting than artificial neural networks (ANNs).

The paper has also shown that deep learning (1D-CNN) is robust to noise and data variation. by showing acceptable levels of accuracy without the need for preprocessing (cleaning) of the vibration data and by learning complex patterns in the signal.

As the quantity of data available expands over time, deeper CNNs may be constructed, resulting in higher levels of feature representation. The model's accuracy can be improved if this is achievable.

CONFLICT OF INTEREST

The authors do not have any personal or financial interests.

ACKNOWLEDGEMENTS

We would like to thank God for everything, especially for the gift of life. We are also grateful to our families for their love and support. Finally, we would like to acknowledge the Addis Ababa Institute of Technology for providing us with the resources and facilities that we needed to complete this research, especially the mechanics lab.

REFERENCES

- [1] Cerrada, M., Sánchez, R.V., Li Chuan, Pacheco, F., Cabrera D., Oliveira J.V.D. and Vásquez, R.E., “*A Review on Data-Driven Fault Severity Assessment in Rolling Bearings*”, Mechanical Systems and Signal Processing, Vol. 99, 2018, p. 169-196.
- [2] Bahrudin, H. and Softic, S., “*Explainable AI in Manufacturing: A Predictive Maintenance Case Study*”, Springer International Publishing, 2020, doi:10.1007/978-3-030-57997-5_8.
- [3] Daniyan, I., Muvunzi, i., Mpofo, K., Oyesola, M., Ramatsetse, B. and Adeodu, A.,” “*Artificial Intelligence System for Enhancing Product’s Performance During its Life Cycle in a Railcar Industry*”, Procedia CIRP, 2021.
- [4] Kaiser, K., and Gebrael, N., “*Predictive Maintenance Management Using Sensor-Based Degradation Models*”, IEEE Trans Syst Man, Cyber Part Systems Humans 2009;39:840–9. doi:10.1109/TSMCA.2009.2016429, 2009.
- [5] Coleman, C., Damofaran, S. and Deuel E., “*Predictive Maintenance and the Smart Factory*”, Deloitte University Press, 2017.
- [6] Zhang, W., Peng, G., Li, C., Chen, Y. and Zhang, Z., “*A New Deep Learning Model for Fault Diagnosis with Good Anti-Noise and Domain Adaptation Ability on Raw Vibration Signals*”, Sensors, 2017
- [7] Yan, L., Yoshua, B, and George, H., “*Deep Learning*”, Nature, vol. 521, no. 7553, 2015, p. 436.
- [8] Haiqin, Q., Kejun, X. and Likun, R., “*Rolling Bearings Fault Diagnosis via 1d Convolution Networks*”, IEEE 4th International Conference on Signal and

- Image Processing (ICVIP), pp. 617–621, 2019.
- [9] Dean, L., Vincent, S., Rick C. and Charles Y., “*Convolutional Neural Net and Bearing Fault Analysis*”, *Semantic Scholars*, vol. 1, 2016.
- [10] Guo, X., Shen, C. and Chen, L., “*Deep Fault Recognizer: An Integrated Model to Denoise and Extract Features for Fault Diagnosis in Rotating Machinery*”, *Applied Sciences*, vol. 7, no. 1, 2017.
- [11] Dhira,j N. and Jongwon, S., “*Bearing Fault Detection and Diagnosis Using Case Western Reserve University Dataset with Deep Learning Approaches*”, *EEE Access*. 8. 9315-93178, 2020.
- [12] Wade, A.S. and Robert, B.R., “*Rolling Element Bearing Diagnostics Using the Case Western Reserve University Data. a Benchmark Study*”, *Mechanical systems and signal processing*. Vol. 72,2016, pp. 303-315.
- [13] Mohammad, M. and Mohammad, S.I., “*Rolling Element Bearing Fault Detection and Classification Technique Using Vibration Signals*”, *Engineering Proceedings* ,vol. 27, no. 1, 2022. <https://doi.org/10.3390/ecsa-9-13339>, 2022.
- [14] Junjie, D., Gege L. and Caidan, Z., “*A New Bearing-Fault Classification Method Based on Deep Learning*”, 15th International Conference on Computer Science & Education (ICCSE), Delft, Netherlands, 2020, pp. 191-196.
doi:10.1109/ICCSE49874.2020.9201672.
- [15] Ahmad S., Xu-Cheng, Y. and Waheed, Y.R., “*Robust Feature Extraction on Vibration Data Under Deep-Learning Framework: An Application for Fault Identification in Rotary Machines*”, *International Journal of Computer Applications*, vol. 167, no. 4, 2017, pp. 37-45.
- [16] Yin, Z. and Hou, J., “*Recent Advances on Svm Based Fault Diagnosis and Process Monitoring in Complicated Industrial Processes*”, *Neurocomputing*, vol. 174, 2016,pp. 643–650.
- [17] Guo, X., Chen, L. and Shen, C., “*Hierarchical Adaptive Deep Convolution Neural Network and its Application to Bearing Fault Diagnosis*”, *Measurement*, vol. 93, 2016, pp. 490–502.
- [18] Sun, W., Shao, S., Zhao, R., Yan, R., Zhang, X. and Chen, X., “*A Sparse Auto-Encoder-Based Deep Neural Network Approach for Induction Motor Faults Classification*”, *Measurement*, vol. 89,2016, pp. 171–178.
- [19] Sawaqed, S. and Alrayes, M., “*Bearing Fault Diagnostic Using Machine Learning Algorithms*”, *Progress in Artificial Intelligence*, vol. 9, 2020, pp. 341–350.